Dynamic Fragmentation of Natural Ceramic Tiles: Ejecta Measurements and Kinetic Consequences

James D. Hogan[a,b], John G. Spray[b], Robert J. Rogers[a], Gregory Vincent[c], Markus Schneider[c]

[a]*Department of Mechanical Engineering, University of New Brunswick, Fredericton, New Brunswick E3B 5A3, Canada*
[b]*Planetary and Space Science Centre, University of New Brunswick, Fredericton, New Brunswick E3B 5A3, Canada*
[c]*ISL, 5 rue du Général Cassagnou, 68300 Saint-Louis, France*

Abstract

Velocity and size measurements of ejecta derived from impacts of railgun-launched projectiles into 10 mm thick gabbro tiles are examined. Fragmentation of the target and the ejecta velocity field are found to be governed by Hertzian fracture and the transfer of kinetic energy to the target. Over 90 % of the total kinetic energy is contained above the average ejecta velocity and greater than 95 % in angles bounded by Hertzian fracture. Log-normal distributions of the ejecta revealed that the kinetic energy transfer from projectile to ejecta is an organized process that spans over four orders of magnitude. The ejection angle that contains the most total kinetic energy coincides with the primary ejection angle, indicating the importance of larger plate-like fragments on the fragmentation process. Approximately 11 % to 16 % of energy to the target (initial - final kinetic energy of the projectile) is converted to the kinetic energy of fragments when the projectile does not perforate the target ($\leq$ 52 J). The conversion to fragment kinetic

Email address: jd.hogan@unb.ca (James D. Hogan)

energy increases near-linearly to $\sim$50 $\%$ at an incoming projectile energy of 305 J. This indicates the importance of this energy conversion mechanism under these experimental conditions.
Keywords: particle tracking velocimetery, dynamic fragmentation, ejecta measurements, railgun, Hertzian fracture, impact testing

---

1. Introduction

The quasi-static fracture of linear elastic-plastic and linearly viscoelastic materials are quite well understood [1–7]. Fracture occurs if the stress at a crack tip exceeds the cohesive forces between atoms or molecules. Dynamic fracture, where inertia effects are important in crack propagation mechanics, is less well understood. This is due to the complex interaction of varying spatial and temporal length scales that span many orders of magnitude. Dynamic fragmentation is a spatially and temporally discrete process governed by flaws (inherent and random), material properties (e.g., toughness, hardness) and structure (e.g., grain orientation and size) [8]. The dynamic fracture and fragmentation of solids have been an area of continued interest since the early works by Mott [9, 10], and they remain an active area of research [11–18]. The dynamic fragmentation of natural brittle materials is the subject of this paper.

Impact testing has been used to study the fragmentation of brittle materials (e.g., ceramics) since the development of high-speed launchers (e.g., solid propellant launchers, light-gas guns) in the 1950's [19–24]. High-speed impact testing can be accomplished using, for example, solid propellant guns (200 m/s to 2.75 km/s [25]), single- and two-stage light-gas guns (300 m/s to 7.5 km/s [25]), and electromagnetic railguns (10 m/s to 8 km/s [26–29]). Railgun launch tech-

nology is especially desirable because it has a relatively low operational cost and is able to achieve higher theoretical velocities and efficiencies than conventional chemical propulsion systems [30].

Applications for impact testing include evaluating the ballistic performance of ceramic-metal shielding systems [31–35] and simulating colliding planetary bodies in small-scale laboratory experiments [36–39]. This research has yielded valuable information on the mechanisms governing fragmentation through the predominantly qualitative post-experiment analysis of fragments [13–15, 40] and the examination of fracture surfaces using, for example, scanning electron microscopy [40] and transmission electron microscopy [41, 42]. Real-time measurements of the dynamic fragmentation of brittle materials have been less studied due to the difficulty of collecting measurements (e.g., time resolution, triggering) [43, 44]. Examples of real-time measurements include velocity interferometry (VISAR) to determine equations of state [45–47] and velocity measurements of ejected fragments [19–23, 44, 48–51]. In the present work, velocity and size measurements of ejecta are recorded to investigate the dynamic fragmentation of gabbro tiles.

Ejecta are generated through the dynamic tensile failure of the target material via energy and momentum transfer from the impactor to the target. Laboratory studies concerned with ejecta velocity distribution measurements have mainly focused on planetary impact scenarios involving, for example, basalt [44, 49], loose quartz and sand targets [50, 51], and regolith-like powders [20]. These studies have primarily focused on quantifying crater formation [52–55], the effect of porosity [56], scaling [51–54] and corresponding ejecta size-velocity distributions [19–23, 48, 57–59].

Velocity measurements of ejecta have been obtained using various methods in the past. Examples include: hand-tracing vector fields onto photographs [49] and using post-experiment measurements of spatial distributions of mass to back-calculate necessary velocities [43]. While these investigations have offered insight into these catastrophic events, the ambiguity of these methods has not enabled capture of a comprehensive set of velocity-size measurements to yield reliable statistics. Knowledge of these relationships enable reconstruction of the fragmentation process through analysis of fragment velocities, and provide a deeper understanding of the underlying kinetics of, for example, impact cratering and planetary formation, ballistic protection, and the dynamic fragmentation of brittle materials.

More recently, particle tracking velocimetry (PTV), which is analogous to particle image velocimetry (PIV) used in fluids research, has been implemented to track the motion of multiple fragments over several high-speed image frames in highly cluttered debris fields [51]. Tracking of all individual fragments is difficult because of the cluttered nature of the debris field and the inherent difficulty in developing associated computational algorithms.

This paper investigates the velocity-size distributions and associated kinetic energy contribution of low-speed impacts (26-100 m/s) into gabbro tiles (10 mm thick). An electromagnetic railgun was used as the launching platform. Low-speed tests of this kind have not received attention in the literature, but are more tractable since a lower number of distinct fragments are generated in comparison to higher energy tests. The distribution of kinetic energy among ejecta velocities, angles, sizes and kinetic energies are presented. Fragment size distributions are examined and the relationship between kinetics and damage is explored.

2. Experimental Setup and Analysis Methods

The impact tests were performed at the French-German Research Institute of Saint-Louis (ISL), France, to investigate the dynamic fracture of gabbro tiles (150 mm by 150 mm and 10 mm thick). The density is estimated at 3,200 kg/m^3. Gabbro is a coarse grained, intrusive mafic igneous rock consisting of plagioclase, pyroxene, amphibole, and olivine. Gabbro tiles were chosen because they are relatively homogeneous, there is an abundant supply, and they serve well as a starting material for future tests. In addition, the material used is dark in colour, allowing the fragments to be more easily distinguished by the tracking software, as compared to lighter coloured rocks. The target configuration is shown in Figure 1a. The tile is sandwiched between two plywood plates and is secured with four bolts on each side of the tile. The projectile used to fragment the tile was cast from aluminum and had a mass of 62 g (Figure 1b). The projectile was 30 mm in length and had a hexagonal cross-section with 20 mm between diagonal vertices. A single copper brush passes through the projectile to enable conduction with the rails. Impact velocities of 26 m/s to 100 m/s were obtained using the SR 3/60 electromagnetic railgun [60], corresponding to kinetic energies at impact of 21 J to 305 J. Estimates of strain rate limits (velocity/thickness) of $> 2.6 \times 10^3$ indicate these tests are dynamic. Values for all trials are displayed in Table 1.

A Photron APX Ultima video camera filming at a 8 kHz frame rate captured fragment trajectories at the rear of the targets. Two high-powered lamps are used to back-illuminate the particles. Proper lighting is critical with such an experimental setup. A tracking algorithm written in Matlab [61] is implemented to track ejecta larger than 0.8 mm (length of two pixels determined by resolution of the camera) over multiple high-speed camera images. The high degree of temporal

resolution available by the camera allows fragments to be tracked with certainty over the course of their path.

Ejecta velocity was obtained by first determining the location of the fragments in one frame and then matching probable locations through cross-correlation in subsequent frames. Fragments are assumed to mainly move in the positive x-direction (horizontal) and expected paths are estimated based on previous frames. Results reported here are taken for three consecutive frames, as little variation was found when a greater number of consecutive images were used. Individual fragments were then identified by sizes and displacements, thereby yielding velocity. As validation, some particle-tracking measurements were compared with hand-traced measurements. Sizes agreed within 8 $\%$, velocity 3 $\%$ and spatial position within 1 $\%$.

Individual ejecta fragments were sized and counted at Malvern Instruments, Westborough, MA, using a Parsum IPP 70-S gravity-feed probe with operating range of 10 μm to 6 mm. Secondary electron (SE) and back-scattered electron (BSE) images of the fracture surfaces were obtained using a Hitachi SU-70 analytical Field Emission Scanning Electron Microscope (FESEM).

3. Experimental Results

3.1. Qualitative analysis of the ejecta field

The qualitative nature of the debris cloud evolution are examined in Figures 2 and 3 for impact energies of 21 J and 305 J, respectively. These are selected to illustrate observed behavioral trends in fragmentation mechanisms. Principal axes and scales are defined in all figures. Shown in Figure 2 is the 21 J case. After 3.75 ms, the debris cloud remains intact. Spall fragments are highlighted in the

figure. These fragments are inferred to be spall because they have much higher velocities than their neighboring fragments and they are plate-like in nature [22, 62]. In fact, many of the larger fragments in Figure 2 are plate-like in nature, suggesting the formation of these fragments is through tensile failure at the free surface and not through another mechanism, such as cascading fracture (i.e., the process of crack propagation and bifurcation from larger lengths to smaller scales) or rupture.

After 10 ms (Figure 2b), a zone of smaller fragments follows the plate-like fragments. These are believed to be formed via comminution and crushing ahead of the projectile and are similar to the zone of highly crushed material observed in many other impact tests into semi-infinite targets [22, 62]. Another zone of fragments follows the comminuted zone. These are believed to occur through rupture of the target as a result of its rapid deformation from the transfer of energy and momentum from projectile contact. Rupture of the target is assumed due to the thin target thickness. Fragment sizes within this group are the most variable among the described fragmentation mechanisms (highlighted in Figure 2b). The evolution of the debris after 20 ms is shown in Figure 2c. The projectile now has a negligible velocity indicating that nearly all of its kinetic energy has been transferred to the target. The evolution of the comminuted fragments is better observed in this image.

Figure 3 shows the evolution of the debris cloud for an impact energy of 305 J. There is a noticeable increase in the number of fragments (Figure 3a). The larger fragments formed at the rear of the target through tensile cracking (spallation) are decreased in size. Next, shown in Figure 3b is the evolution of the debris cloud 6.25 ms after impact. Fast moving smaller fragments and slower moving

larger fragments formed via rupture are highlighted in the figure. Finally shown in Figure 3c is the evolution of the debris field at 10 ms following impact. The comminuted fragments in the debris field become more numerous and increasingly spatially scattered.

3.2. Examination of target and fragment photographs

Next, the nature of the target and the larger fragments for the 21 J and 305 J are shown in Figure 4. The target pieces, which are not ejected during impact and contain surfaces of radial and circumferential through-cracking, are shown on the left and examples of the larger fragments, which comprise plate-like fragments and those which form a cone, are shown in the right hand images. Estimates of all fragments for the 21 J and 305 J cases reveal cone angles of 22 to 27°, with little variation observed for either case. Worth noting is that the larger pieces have a thickness equal to the target target (i.e., 10 mm). This is used later as a rule to estimate fragment mass tracked by the algorithm.

3.3. Quantification of the ejecta field

The velocity fields for the 21 J, 112 J, 163 J, 220 J, and 305 J experiments are shown in Figure 5. Points on the plots correspond to measured ejecta. These energies are selected to represent the evolution of the ejecta field as the impact energy is increased. Note that three cases (112 J, 220 J, and 305 J) are plotted for v_y vs v_x in (a1) and two (21 J and 163 J) are plotted in (a2). Corresponding ejection angles (defined as the arctan(v_y/v_x)) with resultant velocity are shown in Figure 5b.

Results will be discussed with respect to the ejecta angle and resultant veloc-

ity [1] (Figure 5b), with the velocity (v) field in (a1,2) used for visualization. For v<10 m/s, $|\theta|$ is bounded by $\sim$50°. The bounds on $|\theta|$ increases to $\sim$25° at approximately the average velocity for impact energies $>$ (indicated in Figure 5b with bands). The average velocity increases from 7 m/s at an impact energy of 21 J to 31 m/s at 305 J.

Shown in Figure 6 is the total percentage of the initial kinetic energy (IE) that is transferred into the target. This is obtained by measuring the projectile velocity following perforation of the target. The energy not contained in the projectile kinetic energy is assumed to be completely transferred into the target. 100 $\%$ of the energy was transferred (i.e., no perforation) to the target for the $\leq$ 52 J cases. Perforation occurs for >98J (Figure 6) and the total percentage of kinetic energy into the target decreases to 44 $\%$ for an impact energy of 305 J. Perforation is predicted for impact energies greater than about 90 J. A limit of 44 $\%$ of the energy is not likely reached and the decreasing trend is believed to continue as the impact energy is increased beyond 305 J.

The ratio of tracked and collected mass is used to scale fragment numbers and, by extension, size, mass, kinetic energy, and momentum distribution. Mass estimates for the tracked fragments are obtained by multiplying the density with the projected area (determined by the algorithm) and the minor axis (axis normal to longest axis) for minor axes $\leq$10 mm (i.e., the target thickness). Minor axes are set to 10 mm for those fragments with minor dimensions >10 mm. This assumption is reasonable based on Figure 4, where larger fragments are commonly the thickness of the target. The mass obtained from the algorithm, mass collected following each experiment, their ratios and the non-scaled total number of fragments

[1] It is assumed that v_z=v_y.

measured by the algorithm are displayed in Table 2.

3.4. Normalized fragment count and kinetic energy distribution with ejection angle

Shown in Figure 7 are histogram distributions of normalized count (bin summation divided by total number) with ejection angles for impact energies of 45 J, 112 J, 220 J, and 305 J. The distribution of fragments with ejecta angles for an impact energy of 45 J is shown in Figure 7a. The distribution is near-normal about -7° at a peak of $\sim$11%. There is also a peak at approximately 45 J that corresponds to slow moving fragments. These are likely crushed ahead of the projectile. Near-symmetry about a negative angle of $<$ -5° is consistent for all impact energies $\leq$ 52 J, with no clear trend in peak value observed. The extremities of this distribution are -45° and 28°.

Shown in Figure 7b is the 112 J case. The distribution is symmetric about -3° and the peak remains at approximately 10 %. The distribution of fragments becomes increasingly symmetrical about an ejection angle of 0° as the impact energy is increased to 220 J (Figure 7c) and 305 J (Figure 7d) indicating that the flow centre becomes parallel with the projectile impact angle.

Shown in Figure 8 are histogram distributions of the % of the total of fragment KE for grouped ejection angles. Grouping the energy enables evaluation of the directional dependence of the kinetic energy transfer from the target. Trends in momentum are consistent with those for kinetic energy throughout the paper and are not discussed further for brevity. The 45 J case is shown in Figure 8a. The primary group at an ejection angle of -7° contains $\sim$45 % of all KE and angles between 0 and -10° contain $\sim$80 % of the total kinetic energy. The primary group contains $>$35 % of the total kinetic energy for pre-penetration impact energies and

negative ejecta angles contain $\sim$90 $\%$.

The contribution of the primary group decreases to 20 $\%$ as the impact energy is increased to 112 J (Figure 8b). The peak in the kinetic distribution is centred at -3°. The total contribution of the negative ejecta angles corresponds to $\sim$65 $\%$. The primary three groups contain $\sim$63 $\%$ and the distribution is more closely centred about 0° for the 220 J case (Figure 8c). The total contribution among the negative ejecta angles corresponds to 58 $\%$ of the total kinetic energy. Lastly, shown in Figure 8d is the 305 J case. The distribution is centred about 0° and the primary group contains 20 $\%$ of the total KE. Approximately 95 to 98 $\%$ of the total kinetic energy is captured between $\pm$25° for all impact energies.

3.5. Normalized count and kinetic energy contribution of major axis dimension, and mass contribution to each mass group

Shown in Figure 9a and b are the distributions for the normalized count of major axis dimensions (defined as the longest spanning dimension) for impact energies of 45 and 305 J, respectively. Distributions become increasingly skewed towards smaller fragments as the impact energy is increased, with 40 $\%$ of the distribution being composed of fragments $<$2.7 mm for the 45 J case and 46 $\%$ of the total fragments recorded for the 305 J case.

Shown in Figure 9c and d is the percentage of the total kinetic energy for each major axis dimension for impact energies of 45 and 305 J. All distributions are skewed to the larger size fragments. Major dimensions $>$ 10 mm contain 68 $\%$ of the total fragment kinetic energy for 45 J, 65 $\%$ for 112 J, 56 $\%$ for 220 J and 45 $\%$ for 305 J. The decreasing contribution of kinetic energy is a consequence of the size shift to the smaller scales and associated re-distribution of kinetic energy towards these sizes.

Shown in Figure 9e and f are the % contribution of the total mass for each grouped mass. For an impact energy of 45 J, distribution peaks for masses >470 mg range from 7 % to 15 % and contain 66 % of the total mass. Each mass group >380 mg contains approximately 9 % of the total mass, with the total of the sum of these groups is equal to 68 % for the 305 J case (Figure 9f).

3.6. Normalized count of ejecta velocity and contribution of mass and kinetic energy

Figure 10a-d shows the normalized distribution of ejecta velocities for impact energies of 45 J to 305 J. Post-impact projectile (v_p) and average velocities (v_{avg}) are indicated in the figures. The distribution for the 45 J case (Figure 10a) is skewed towards the lower ejecta velocities, with the majority of the fragments having velocities <16 m/s. The average (v_{avg}) and maximum velocities for the 45 J case are 7 m/s and 33 m/s, respectively. The distributions expand towards higher velocities when the impact energy is increased to 112 J (Figure 10b). The peak percentages range from 4 % to 7 % for velocities greater than the average velocity. The average and maximum velocities for the 112 J case are 18 m/s and 46 m/s, respectively. When the impact energy is increased further to 176 J, the velocity distribution further expands towards higher velocities and the counts are re-distributed to peaks of 3 % to 5 % for groups $>v_{avg}$. The average and maximum velocities for the 176 J case are 24 m/s and 64 m/s, respectively. Increasing the impact energy to 305 J, results in a further expansion of the sub- v_{avg} fragments to higher velocities. Again, percentages are similar for higher ejecta velocities at peaks of 2 % to 4 % for velocities groups greater than the average velocity. The average and maximum velocities are 31 m/s and 97 m/s, respectively. Shown in Figures 10e and f are the average and maximum velocities for all impact tests.

Shown in Figure 11 is the distribution of kinetic energy versus fragment velocity groups. For all cases, ejecta velocities greater than the mid-range velocity contain the bulk of the kinetic energy. The total percentage of kinetic energy contained above v_{avg} is shown in Figure 11e. For impact energies <52 J, 91 $\%$ (at 21 J) to 96 $\%$ (at 52 J) of the total kinetic energy is contained above the average velocity. There is a decrease to 77 $\%$ when the projectile perforates the target at 98 J. The kinetic energy contributions rises to 90 $\%$ as the impact energy is increased to 305 J.

3.7. Normalized count and contribution of kinetic energy to kinetic energy

Shown in Figure 12 is the normalized distribution of fragment kinetic energies. Shown in Figure 12a is the 45 J case. The distribution is near log-normal about a median value of 3.0×10^{-4} J. Median values of approximately 3.0×10^{-4} J to 5.6×10^{-4} J are consistent for impact energies of $\leq$ 52 J. The log-normal nature of the curve indicates that the kinetic energy transfer to individual fragments is a coherently organized process, unlike individual distributions of velocity or mass, over six orders of magnitude observed in these experiments.

Further increasing the impact energy results in an increase in the distribution median (2.1×10^{-3} J at 144 J and 4.1×10^{-3} J at 305 J). Distributions for the higher impact energies are log-normal over four orders of magnitude, with the gaussian nature of the distribution breaking down for kinetic energies of $<10^{-4}$ J. Fragments $<10^{-4}$ J are likely crushed and comminuted ahead of the projectile. A summary of the medians in the distributions is shown in Figure 12f with a power law-curve for the impact energies $>$ 98 J. Median kinetic energies increase for increasing impact energy, with a great rate of increase being observed for impact energies $>$ 52 J.

Shown in Figure 13 is the total percentage contribution of kinetic energy among kinetic energy groups. The 45 J experiment is shown in Figure 13a. Energies ranging from 0.06 J to 1 J contain $\sim$78 $\%$ of the total kinetic energy, with the largest group $\sim$40 $\%$. Similar characteristics are observed for impact energies of $\leq$ 52 J.

The 112 J case is shown in Figure 13b. Recall perforation is first observed near this impact energy. The primary group has decreased significantly (18 $\%$ at 112 J from 40 $\%$ at 45 J) and the energy has been redistributed evenly among ejecta energies of 0.06 J to 2.5 J. They contain $\sim$82 $\%$ of the total kinetic energy. The similarity of peak energies at $\sim$17$\%$ and the summation of energies $>$0.06 J at 80$\%$ remains consistent for impact energies of 144 J (Figure 13c) to 305 J (Figure 13d). Results are similar for the momentum, where $>$76 $\%$ is captured in the largest momentums.

Shown in Figure 13e is the total percentage of energy transferred to the target that is converted to ejecta kinetic energy. Note that these are obtained by extrapolating algorithm measurements using a ratio of tracked and recovered mass. Approximately 11 $\%$ to 16 $\%$ of energy to the target is converted to kinetic energy of fragments for incoming projectiles energies of $\leq$ 52 J. No perforation occurs for these cases. The $\%$ conversion to kinetic energy increases to $\sim$50 $\%$ at an incoming projectile energy of 305 J. Percentages are slightly lower for momentum (Figure 13f). Approximately 2 $\%$ to 13 $\%$ of momentum to the target is converted to momentum of fragments for incoming projectiles momentums of $\leq$ 3.5 kg m/s. The values steadily increase to 45 $\%$ at 6.1 kg m/s. Overall, incoming project kinetic energy and momentum partitioning into fragment kinetic energy and momentum represents a notable conversion for impacts into thin ceramic tiles and

become more dominant as the impact momentum is increased.

3.8. Damage Features

This section explores associated consequences of the dynamic fragmentation of the gabbro tiles using scanning (SE) and backscatter electron (BSE) microscopy. Damage features are attributed to multiple interactions of fragments and fracture propagation. Shown in Figure 14 are typical fracture surfaces for impact energies of (a) 45 J and (b) 305 J. Fracture surfaces are rough, with the higher impact energy containing, on average, more deeper fractures (highlighted in Figure 14b). Limited fracture along cleavage planes (indicated in Figure 14a) is observed. Analysis of the fracture surfaces at this scale indicate the mode of fracture and fragmentation under such experimental conditions is primarily through rupture.

Micro-scale fracture surfaces located on a fragment at the projectile impact point are examined in Figures 14c and d. The surface is primarily covered in melt, indicating that temperatures of at least 1,373 K [63] are achieved locally due to frictional heating. Large frictional forces also enhance comminution of the target material ahead of the projectile to generate the sub 1 mm fines observed previously. Folds of plagioclase melt approximately 10 μm in length are also observed (Figure 14d), indicating the spatial extent of shearing of contacted surfaces.

Analysis of the damage is extended here by investigating intra-fragment fracture (Figure 15). A sub-1 mm fragment is shown in Figure 15a. The fragment is composed of different minerals (indicated by the color contrast in the BSE image). The edge of the fragment, which is its surface, is jagged and contains limited cleavage fracture. There are few noticeable intra-fragment fractures (highlighted in the image), which primarily occur along grain boundaries.

An image of micro-scale fracture behavior is shown in Figure 15b. Large

transgranular fractures, likely generated from tensile stress [64], are indicated in the figure. Thinner fractures are observed within the plagioclase grain. All cracks emanate from the surface of the fragment. The complex array of fractures helps to form secondary fragments from the parent fragment. These fractures help to dissipate energy through the generation of new surface area and via associated elastic, plastic and thermal effects. Visually-thicker fractures are believed to be a result of tensile failure of adjacent grains under stable crack-forming conditions. Thinner straighter tensile fractures are assumed unstable and a result of interactions (e.g., contact, abrasion) with adjacent fragments during early stages of the impact event. Both are highlighted in Figure 15b.

Micro-scale damage in plagioclase is examined further in Figures 15c to f. Energy dissipation through heat and plastic deformation at the micro-scale represents a significant component of the energy [63]. Shown in Figures 15c is an example of highly comminuted fragments. The interaction of rough fracture surfaces and surface asperities through shearing leads to the degradation of these surfaces and the formation of sub-20 μm fragments. Comminution is very energy intensive process [63].

Micro-scale processes are not limited to fracture. Significant plastic deformation of the cleavage planes in plagioclase up to 5 μm into the grain surfaces is a product of fragment interaction through shearing (Figure 15d) This contributes to overall energy dissipation within the gabbro. Shown in Figure 15e is evidence of micro-scale localized plastic deformation via necking. The formation of plagioclase strings is a result of high strain-rate loadings at inter-granular surfaces brought on by rupture of the target body. Lastly, shown in Figure 15f is evidence of micro-gouging in a plagioclase surface. Energy-dispersive X-ray spectroscopy

confirms traces of olivine in the gouges, which is on average harder than plagioclase (H_{v-oli}=6.5-8.4 GPa and H_{v-pla}=6-6.5 GPa [63]). The path of the gouge is non-linear, indicating the complex nature of the stress field imposed on fragments through interactions with adjacent particles of polyphase composition and complicated surface asperities.

4. Summary and Implications

The fragmentation of gabbro tiles was investigated for impact energies of 21 J to 305 J. Failure at the rear of the target was primarily due to the propagation of circumferential and radial through-cracking. Various fragmentation mechanisms were identified through evaluation of the debris cloud: plate-like spalled fragments [22, 62] at rear of target, comminution ahead of the projectile [62], and rupture of the remaining target. Multi-scale surface features confirmed rupture as the primary mode of fragmentation.

Ejecta were observed to be bounded by fracture cones with apex angles of 22° to 27°. The formation of cones in the targets are commonly observed in impact tests [18] and is attributed to Hertzian fracture. Hertzian cone cracks and their trajectories are defined by the stress field in the body at impact [64, 65]. Crack trajectories, defined here as the outer edge of the cone, will follow the direction of maximum energy release [64]. For asymmetric loading in non-uniform stress fields, these trajectories do not necessarily correspond with the normal to the maximum tensile stress [64].

The relationship between ejecta angle ($|\theta|$) and velocity was evaluated. $|\theta|$ is bounded by $\sim$25° for velocities $>$ v_{avg}. This angle coincides with the Hertzian fracture zone and indicates the dependence of ejecta angle and average velocity

on Hertzian fracture and the commonality of the fragmentation process. From the qualitative images, the regions bounded by $<\mathrm{v}_{avg}$ primarily contain fragments formed from rupture and comminution. These fragments are in close spatial proximity and are assumed to be formed during the earlier stages of the impact process [22, 62]. The low velocities for these fragments is a measure of the residual velocity following fragmentation and particle interaction. Alternatively, the region bounded by $>\mathrm{v}_{avg}$ contains plate-like fragments and ruptured fragments and are fewer in number.

The implication of ejecta angles being governed by the direction of maximum energy release of the stress field (i.e., Hertzian fracture) [64] is significant in brittle and granular solid applications, such as impact crater formation. Components of impact cratering stages (e.g., transient cavity, ejecta angle) can be determined using well-known solutions to the stress field (i.e., Hertzian contact mechanics) [65]. For example, ejecta angles can be back calculated from displaced ejecta on planetary and lunar surfaces [51], which provide insight into the stress state of the crater during a hypervelocity impact event. In addition, early and late time stress field solutions [65] may provide a better understanding of the transition from complex to simple craters [66]; a subject not entirely resolved in the impact cratering field.

Ejecta angle distributions reveal a migration away from 0° below the critical perforation energy (estimated as $<$ 90 J). This may be attributed to gravity effects over the measurement window and a lack of momentum and kinetic energy transferred to the ejecta from the projectile. The flow-field direction became increasingly symmetrical about 0° as the impact energy was increased. The flow-field direction coincides with the angle that contains the most kinetic energy. This suggest a directional dependence of fragmentation on the direction of maximum

kinetic energy transfer to the target. Further, distributions of the kinetic energy with ejecta size also indicated that larger sizes contain the bulk of kinetic energy. The larger sizes are inferred as spalled fragments. All together, this indicates that more fragmentation commonly occurs in the spall direction. Approximately 95 to 98 % of the total kinetic energy is captured between $\pm 25^{\circ}$ for all impact energies, indicating a significant shift towards fragments bounded by the Hertzian fracture as the impact energy is increased.

Histogram distributions of the major axis dimension and mass are increasingly skewed towards smaller fragments as the impact energy is increased (40 % of the total number of fragments contained $<$2.7 mm for the 45 J and 46 % for the 305 J). Masses $>$380 mg contain approximately 68 % of the total mass for all impact energies, with each group containing between 8 and 15 %. This is important, because this suggest that they contribute equally to the total fracture energy during the the fragmentation of the tile [2]. Further, this indicates important mass scales that can be implemented in numerical models to capture the bulk of the fragmentation energy.

Major axis lengths $>$10 mm contain 68 % of the total fragment kinetic energy below the critical perforation energy. This consistently decreased following perforation to 45 % at an impact energy 305 J as a consequence of the shift to smaller sizes and associated re-distribution of kinetic energy towards these sizes. The significant contribution of kinetic energy to larger size particles, and those previously observed to be formed at the rear surface of the target, indicate their importance towards kinetic energy transfer and, by extension, their formation through tensile fragmentation. Ejecta size values presented here can also be implemented numer-

[2] According to Kick [67], fragmentation energy was proportional to volume or weight.

ical modelling codes to capture the bulk of the kinetic energy transfer of ejecta.

Trends in the normalized distribution of ejecta velocities reveal a fanning of ejecta velocities greater than the average ejecta. Average and maximum velocities were found to increase, with the average velocity being indicative of the Hertzian fracture zone. For impact energies below the critical perforation velocity, 91 % (at 21 J) to 96 % (at 52 J) of the total kinetic energy is contained above the average velocity and, by association, within the Hertzian cone. Following perforation, a decrease to 77 % of the total kinetic energy for particles above the average velocity was observed. The kinetic energy contributions above the average velocity rises to 90 % at an impact energy of 305 J. The total % contribution of fragmentation energy likely increases following perforation, as significantly more fragments are produced and larger ones become smaller, resulting in a net decrease in the total % contribution of kinetic energy.

Log-normal distributions of the ejecta kinetic energy revealed a coherently organized process (unlike individual distributions of velocity or mass) over the four to six orders of magnitude observed in these experiments. The breakdown of the coherent nature of the fragmentation for lower ejecta kinetic energies following perforation is likely due to crushing at smaller mass and velocities scales. Distribution of KE medians were observed to significantly increase following perforation. The large increase following perforation suggests a threshold condition for individual ejecta kinetic energy to achieve projectile perforation of the target.

Individual ejecta energies $>$0.06 J contain $\sim$78 % of the total kinetic energy, with the largest group containing $\sim$40 % for impact energies below the critical perforation energy. The peak of the primary kinetic energy group decreased to 18 % following perforation. Qualitative analysis of the rear of the target suggests

this is likely a result of increased fragmentation of larger fragments as the impact energy is increased. The net contribution of these larger, faster moving fragments (>0.06 J) remains consistent at 80 to 82 %.

Approximately 11 % to 16 % of energy to the target is converted to kinetic energy of fragments for incoming projectiles energies of $\leq$ 52 J. The % conversion to kinetic energy increases to $\sim$50 % at an incoming projectile energy of 305 J. Overall, incoming project kinetic energy and momentum partitioning into fragment kinetic energy and momentum represents a notable conversion for impacts into thin ceramic tiles and become more dominant as the impact energy/momentum is increased.

5. Concluding Remarks

The role of kinetic energy in the dynamic fragmentation of gabbro tile was examined for impact energies of 21 to 305 J. Approximately 11 % to 16 % of energy to the target is converted to kinetic energy pre-perforation. This increases to $\sim$50 % at 305 J. The conversion of impact energy to ejecta kinetic energy is a coherently organized processes that spans over four orders of magnitude. The primary direction of kinetic energy coincides with the spallation of larger plate-like fragments and governs the fragmentation process. The spallation of fragments from the rear surface of the target contribute 68 % at 21 J and 45 % at 305 J of the total ejecta kinetic energy. Hertzian fracture was found to be an important mechanism governing the average ejecta velocity, with over 90 % of the total kinetic energy contained above v_{avg} and >95 % in angles bounded by Hertzian fracture.

Recent advances in particle sizing technology and high-speed photography

and image processing capabilities have made it possible to study fragmentation phenomena in greater depth. Ejecta quantification is essential for continued development of our theoretical understanding of fragmentation and associated computational model development and verification. The data provided here facilitates a framework to facilitate future studies and should be valuable for verification of analytical and computational models for the dynamic fracture of brittle solids.

Acknowledgements

This work was supported by a Natural Sciences and Engineering Research Council (NSERC) PGS-D scholarship to JDH and funding from NSERC, the Canada Research Chairs program and the Canada Foundation for Innovation to JGS. Planetary and Space Science Centre contribution 73. The authors would also like to thank the efforts and contributions during the experimental phase of the study of Philippe Baumann, David Bluntzer, Yannick Boehrer, and Gregory Vincent at ISL. Suporn Boonsue is also thanked for acquisition of the electron microscope images. Karen Shea is thanked for her continued support in editing the manuscript.

[1] J. R. Rice, Thermodynamics of the quasi-static growth of griffith cracks, Journal of the Mechanics and Physics of Solids 26 (2) (1978) 61 – 78.

[2] G. Francfort, C. Larsen, Existence and convergence for quasi-static evolution in brittle fracture, Communications on Pure and Applied Mathematics 56 (10) (2003) 1465 – 1500.

[3] E. Eberhardt, D. Stead, B. Stimpson, R. Read, Identifying crack initiation and propagation thresholds in brittle rock, Can. Geotech. Journal 35 (1998) 222 – 233.

[4] G. Irwin, Fracture dynamics, Fracturing of Metals (1948) 147 – 166.

[5] G. Iwin, J. Kies, Fracturing and fracture dynamics, Welding Journal Research Supplment.

[6] G. Iwin, J. Kies, Critical energy rate analysis of fracture strength of large welded structures, Welding Journal Research Supplment.

[7] A. A. Griffith, The phenomena of rupture and flow in solids, Philosophical Transactions of the Royal Society of London. Series A, Containing Papers of a Mathematical or Physical Character 221 (1921) 163–198.

[8] D. E. Grady, D. A. Benson, Fragmentation of metal rings by electromagnetic loading, Experimental Mechanics 23 (4) (1983) 393–400.

[9] N. Mott, A theory of the fragmentation of shells and bombs, Technical Report AC4035, United Kingdom Ministry of Supply (May 1943).

[10] N. Mott, Fragmentation of shell cases, Technical Report A189: 300308, Proceedings of the Royal Society (1947).

[11] D. Grady, The spall strength of condensed matter, Journal of Mechanics Physics of Solids 36 (1988) 353–384.

[12] S. Levy, J. Molinari, Dynamic fragmentation of ceramics, signature of defects and scaling of fragment sizes, Journal of the Mechanics and Physics of Solids 58 (1) (2010) 12 – 26.

[13] D. Grady, M. Kipp, The micromechanics of impact fracture of rock, International Journal of Rock Mechanics 16 (5) (1979) 293 – 302.

[14] D. Shockey, D. Curran, L. Seaman, Fragmentation of rock under dynamic loads, International Journal of Rock Mechanics and Mining Sciences and Geomechanics Abstracts 11 (12) (1974) 250.

[15] D. Grady, Length scales and size distributions in dynamic fragmentation, International Journal of Fracture 163 (1–2) (2009) 85–99.

[16] D. Grady, Fragment size distributions from the dynamic fragmentation of brittle solids, International Journal of Impact Engineering 35 (12) (2008) 1557 – 1562, hypervelocity Impact Proceedings of the 2007 Symposium - HVIS 2007.

[17] J. D. Hogan, R. J. Rogers, J. G. Spray, S. Boonsue, Dynamic fragmentation of granite for impact energies of 628 joules, Engineering Fracture Mechanics (0) (2011) –. doi:10.1016/j.engfracmech.2011.10.006.
URL http://www.sciencedirect.com/science/article/pii/S0013794411003

[18] J. D. Hogan, J. G. Spray, R. J. Rogers, S. Boonsue, G. Vincent, M. Schneider, Micro-scale energy dissipation mechanisms during dynamic fracture

in natural polyphase ceramic blocks, International Journal of Impact Engineering 38 (12) (2011) 931 – 939. doi:10.1016/j.ijimpeng.2011.06.004. URL http://www.sciencedirect.com/science/article/pii/S0734743X11001

[19] I. Giblin, New data on the velocity-mass relation in catastrophic disruption, Planetary and Space Science 46 (8) (1998) 921 – 928.

[20] W. K. Hartmann, Impact experiments : 1. ejecta velocity distributions and related results from regolith targets, Icarus 63 (1) (1985) 69 – 98.

[21] H. Melosh, High-velocity solid ejecta fragments from hypervelocity impacts, International Journal of Impact Engineering 5 (1-4) (1987) 483 – 492, hypervelocity Impact Proceedings of the 1986 Symposium.

[22] C. A. Polanskey, T. J. Ahrens, Impact spallation experiments: Fracture patterns and spall velocities, Icarus 87 (1) (1990) 140 – 155.

[23] A. Nakamura, A. Fujiwara, Velocity distribution of fragments formed in a simulated collisional disruption, Icarus 92 (1) (1991) 132 – 146.

[24] A. G. Evans, Impact damage in ceramics, Fracture mechanics of ceramics Proceedings of the International Symposium (1978) 303–331.

[25] L. Chhabildas, L. Davison, Y. Horie (Eds.), High Pressure Shock Compression of Solid VIII: The Science and Technology of High Velocity Impact, Vol. 8 of High Pressure Shock Compression of Solid, Springer, NY, 2005, Chap. 1–3.

[26] L. Holland, Distributed-current-feed and distributed-energy-store railguns, Magnetics, IEEE Transactions on 20 (2) (1984) 272 – 275.

[27] A. Poltanov, A. Kondratenko, A. Glinov, V. Ryndin, Multi-turn railguns: concept analysis and experimental results, Magnetics, IEEE Transactions on 37 (1) (2001) 457 –461.

[28] J. Pappas, D. Piccone, Power converters for railguns, Magnetics, IEEE Transactions on 37 (1) (2001) 379 –384.

[29] M. Schneider, O. Liebfried, V. Stankevic, S. Balevicius, N. Zurauskiene, Magnetic diffusion in railguns: Measurements using cmr-based sensors, Magnetics, IEEE Transactions on 45 (1) (2009) 430 –435.

[30] D. Bauer, Achieving high efficiency with conventional railgun launchers, Magnetics, IEEE Transactions on 31 (1) (1995) 263–266.

[31] D. A. Shockey, A. Marchand, S. Skaggs, G. Cort, M. Burkett, R. Parker, Failure phenomenology of confined ceramic targets and impacting rods, International Journal of Impact Engineering 9 (3) (1990) 263 – 275.

[32] E. S. C. Chin, Army focused research team on functionally graded armor composites, Materials Science and Engineering A 259 (2) (1999) 155 – 161.

[33] E. Strassburger, Ballistic testing of transparent armour ceramics, Journal of the European Ceramic Society 29 (2) (2009) 267 – 273, special Issue on Transparent Ceramics.

[34] D. P. Goncalves, F. C. L. de Melo, A. N. Klein, H. A. Al-Qureshi, Analysis and investigation of ballistic impact on ceramic/metal composite armour, International Journal of Machine Tools and Manufacture 44 (2-3) (2004) 307 – 316.

[35] M. L. Wilkins, Mechanics of penetration and perforation, International Journal of Engineering Science 16 (11) (1978) 793 – 807, special Issue: Penetration Mechanics.

[36] K. A. Holsapple, R. M. Schmidt, On the scaling of crater dimensions 1: Explosive processes, Journal of Geophysics 85 (1980) 7247–7256.

[37] K. A. Holsapple, R. M. Schmidt, On the scaling of crater dimensions 2: Impact processes, Journal of Geophysics 87 (1982) 1849–1870.

[38] J. Walker, S. Chocron, Near-earth object deflection using conventional explosives, International Journal of Impact Engineering 35 (12) (2008) 1473 – 1477.

[39] T. Saito, K. Kaiho, A. Abe, M. Katayama, K. Takayama, Hypervelocity impact of asteroid/comet on the oceanic crust of the earth, International Journal of Impact Engineering 35 (12) (2008) 1770 – 1777.

[40] J. D. Hogan, J. G. Spray, R. J. Rogers, S. Boonsue, G. Vincent, M. Schneider, Micro-scale energy dissipation mechanisms during dynamic fracture in natural polyphase ceramic blocks, International Journal of Impact Engineering.

[41] O. Goltrant, P. Cordier, J.-C. Doukhan, Planar deformation features in shocked quartz; a transmission electron microscopy investigation, Earth and Planetary Science Letters 106 (1-4) (1991) 103 – 115.

[42] P. S. Fiske, W. J. Nellis, M. Lipp, H. Lorenzana, M. Kikuchi, Y. Syono, Pseudotachylites generated in shock experiments: Implications for impact cratering products and processes, Science 270 (5234) (1995) 281–283.

[43] Ejecta velocity distribution for impact cratering experiments on porous and low strength targets, Planetary and Space Science 55 (1-2) (2007) 70 – 88.

[44] D. Gault, E. Heitowit, The partition of energy for hypervelocity impact craters formed in rock, Proc. 6th Hypervelocity Impact Symp (1963) 419–456.

[45] C. S. Alexander, M. D. Knudson, C. A. Hall, High accuracy hugoniot measurements at multi-megabar pressure utilizing the sandia z accelerator, Journal of Physics: Conference Series 215 (1) (2010) 012150.
URL http://stacks.iop.org/1742-6596/215/i=1/a=012150

[46] T. Vogler, W. Trott, W. Reinhart, C. Alexander, M. Furnish, M. Knudson, L. Chhabildas, Using the line-visar to study multi-dimensional and mesoscale impact phenomena, International Journal of Impact Engineering 35 (12) (2008) 1844 – 1852, hypervelocity Impact Proceedings of the 2007 Symposium - HVIS 2007. doi:DOI: 10.1016/j.ijimpeng.2008.07.040.
URL http://www.sciencedirect.com/science/article/pii/S0734743X08001

[47] M. D. Furnish, L. C. Chhabildas, W. D. Reinhart, Time-resolved particle velocity measurements at impact velocities of 10 km/s, International Journal of Impact Engineering 23 (1, Part 1) (1999) 261 – 270.

[48] H. Kamminga, Life from spacea history of panspermia, Vistas in Astronomy 26 (1982) 67 – 86.

[49] A. Fujiwara, A. Tsukamoto, Experimental study on the velocity of fragments in collisional breakup, Icarus 44 (1) (1980) 142 – 153.

[50] D. Braslau, Partitioning of energy in hypervelocity impact against loose sand targets, Journal of Geophysical Research 75 (20) (1970) 3987–3999.

[51] B. Hermalyn, P. H. Schultz, Early-stage ejecta velocity distribution for vertical hypervelocity impacts into sand, Icarus 209 (2) (2010) 866 – 870.

[52] S.-R. H. K. Housen, K.R., Crater ejecta scaling laws: fundamental forms based on dimensional analysis, Journal of Geophysical Research 88 (B3) (1983) 2485–2499.

[53] K. R. Housen, K. A. Holsapple, Ejecta from impact craters, Icarus 211 (1) (2011) 856 – 875.

[54] K. A. Holsapple, K. R. Housen, A crater and its ejecta: An interpretation of deep impact, Icarus 187 (1) (2007) 345 – 356, deep Impact Mission to Comet 9P/Tempel 1, Part 1.

[55] K. T. M. P. T. K. T. Hoerth, F. Schfer, A. Deutsch, Ejecta dynamics during hypervelocity impacts into dry and wet sandstone., 42nd Lunar and Planetary Science Conference.

[56] A. M. Nakamura, K. Hiraoka, Y. Yamashita, N. Machii, Collisional disruption experiments of porous targets, Planetary and Space Science 57 (2) (2009) 111 – 118, catastrophic Disruption in the Solar System, VII Workshop on Catastrophic Disruption in the Solar System. doi:DOI: 10.1016/j.pss.2008.07.027.
URL http://www.sciencedirect.com/science/article/pii/S0032063308002

[57] M. J. CINTALA, L. BERTHOUD, F. HRZ, Ejection-velocity distributions

from impacts into coarse-grained sand, Meteoritics and Planetary Science 34 (4) (1999) 605–623.

[58] P. H. S. Jennifer L. B. Anderson, J. T. Heineck, Asymmetry of ejecta flow during oblique impacts using three-dimensional particle image velocimetry, JOURNAL OF GEOPHYSICAL RESEARCH 108 (5094) (2003) 10.

[59] A. R. S. H. Piekutowski, A.J., Studying small-scale explosive cratering phenomena photographically., Int Congr on High Speed Photogr (Photonics), 12th 97 (1977) 177–183.

[60] S. Hundertmark, G. Vincent, Performance of a hexagonal, segmented railgun, IET Conference Publications 2009 (CP553) (2009) 23.

[61] 2011 Matlab user manual.

[62] H. Melosh, Impact ejection, spallation, and the origin of meteorites, Icarus 59 (2) (1984) 234 – 260. doi:10.1016/0019-1035(84)90026-5.
URL http://www.sciencedirect.com/science/article/pii/00191035849002

[63] J. G. Spray, Frictional melting processes in planetary materials: From hypervelocity impact to earthquakes, Annual Review of Earth and Planetary Sciences 38 (1) (2010) 221–254.

[64] C. Kocer, R. E. Collins, Angle of hertzian cone cracks, Journal of the American Ceramic Society.

[65] F. C. Frank, B. R. Lawn, On the theory of hertzian fracture, Proc. R. Soc. Lond. A 299 (1458) (1967) 291–306.

[66] M. Pilkington, R. A. F. Grieve, The geophysical signature of terrestrial impact craters, REVIEWS OF GEOPHYSICS 30 (2) (1992) 161 – 181.

[67] F. Kick, Das gesetz des proportionalen widerstandes und seine anwendung, Arthur Felix, Leipzig.

List of Figures

List of Tables

Table 1: Impact conditions.

Shot Number	Velocity (m/s)	Projectile Mass (g)	Projectile Momentum (kg m/s)	Projectile KE (J)
154	26	62.2	1.6	21
155	38	62.2	2.4	45
153	40	62.2	2.5	50
152	41	62.2	2.6	52
157	56	62.2	3.5	98
156	60	62.2	3.7	112
159	62	62.2	3.9	120
158	65	62.2	4.0	131
161	68	62.2	4.2	144
167	72	62.2	4.5	161
163	73	61.0	4.5	163
160	73	62.2	4.5	166
162	76	61.0	4.6	176
170	81	62.2	5.0	204
169	85	61.0	5.1	220
165	90	62.2	5.6	252
164	95	62.2	5.9	281
166	95	62.2	5.9	281
168	100	61.0	6.1	305

5.1. Tables

5.2. Figures

Table 2: Mass tracked by the algorithm, mass collected following the experiment and the ratio used to scale the experiments.

Shot Number	Energy (J)	Tracked Mass (g)	Collected Mass (g)	Ratio ($\times 100$)	Pre-scale Frag't Number
154	21	19.8	75.0	26.4	118
155	45	30.8	53.2	58.0	259
153	50	26.2	56.2	46.8	263
152	52	34.9	61.9	56.5	237
157	98	97.1	70.1	138.7	313
156	112	74.8	115.4	65.0	397
159	120	105.6	105.1	100.6	355
158	131	79.9	53.7	148.6	387
161	144	69.0	94.7	72.8	321
167	161	87.9	131.6	66.8	310
160	166	86.7	93.5	92.7	425
163	163	96.7	120.2	80.4	394
162	176	110.7	118.6	93.3	445
170	204	102.1	135.0	75.6	437
169	220	79.4	120.2	66.2	562
165	252	237.2	245.2	96.8	518
164	281	210.3	225.5	93.4	422
166	281	260.8	255.0	102.2	510
168	305	259.4	287.7	90.1	639

Fig1a Exp setup

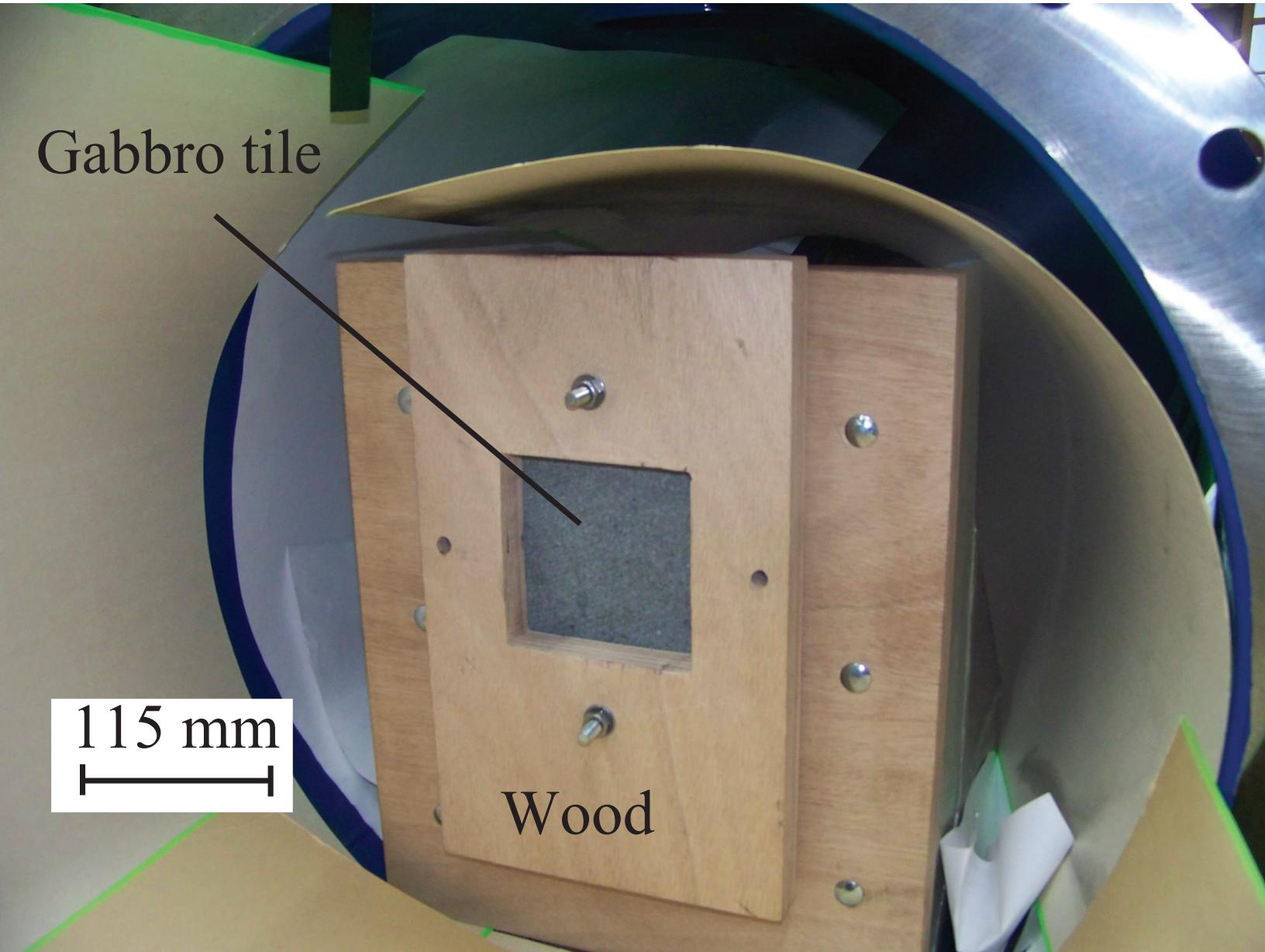

Fig1b Aluminum projectile

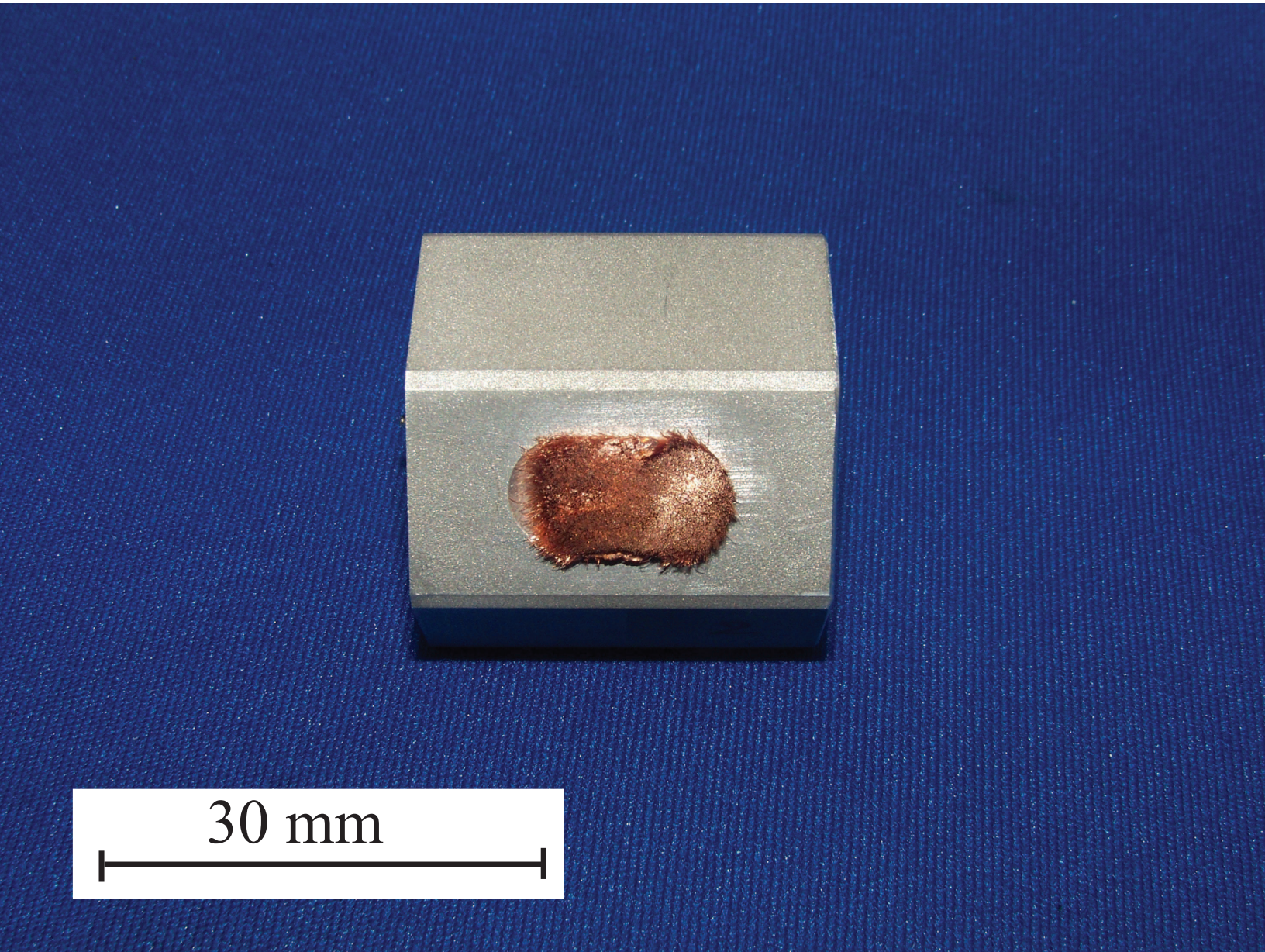

Fig2 Qual nature of debris field for 21 J

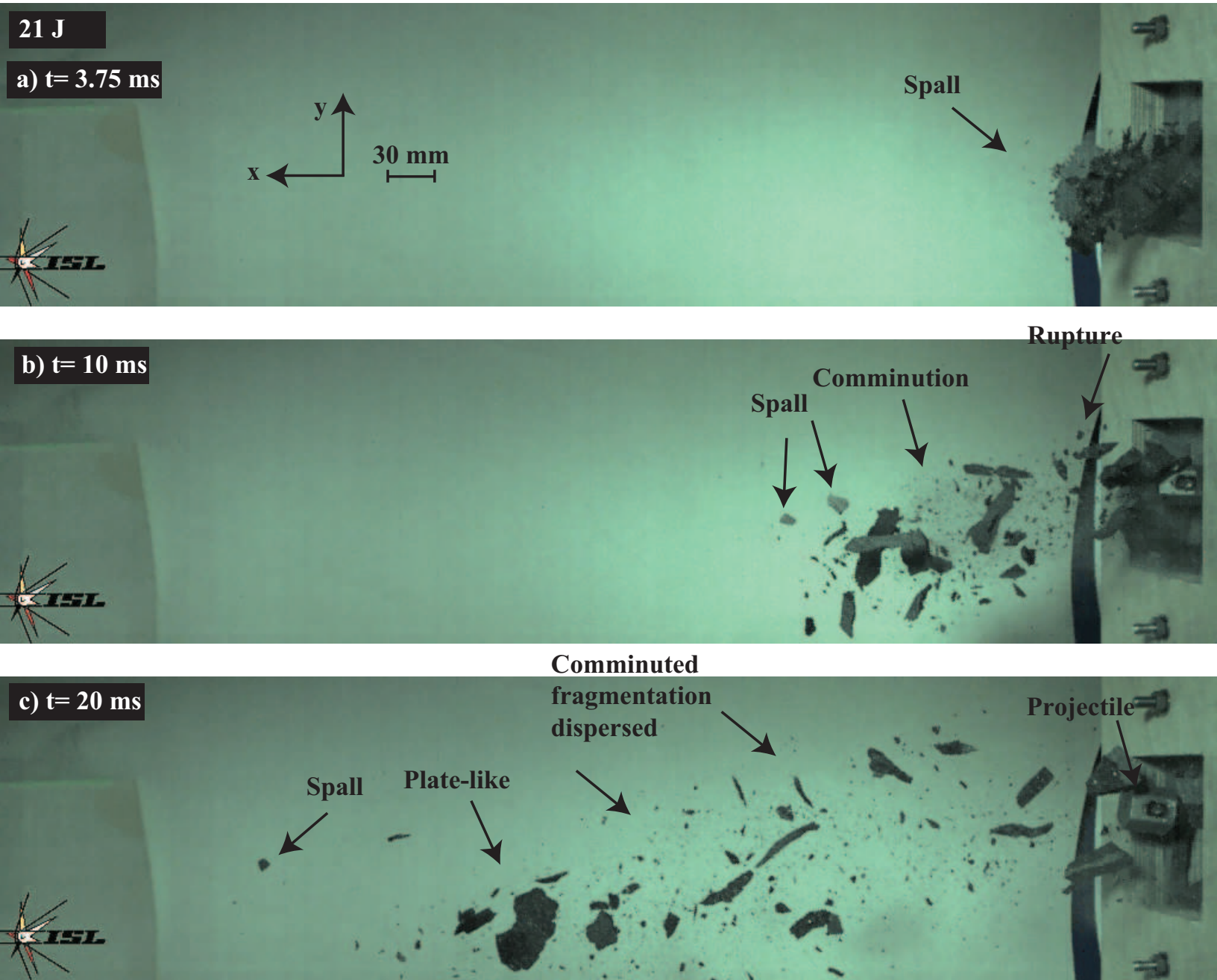

Fig3 Qual nature of debris field for 305 J

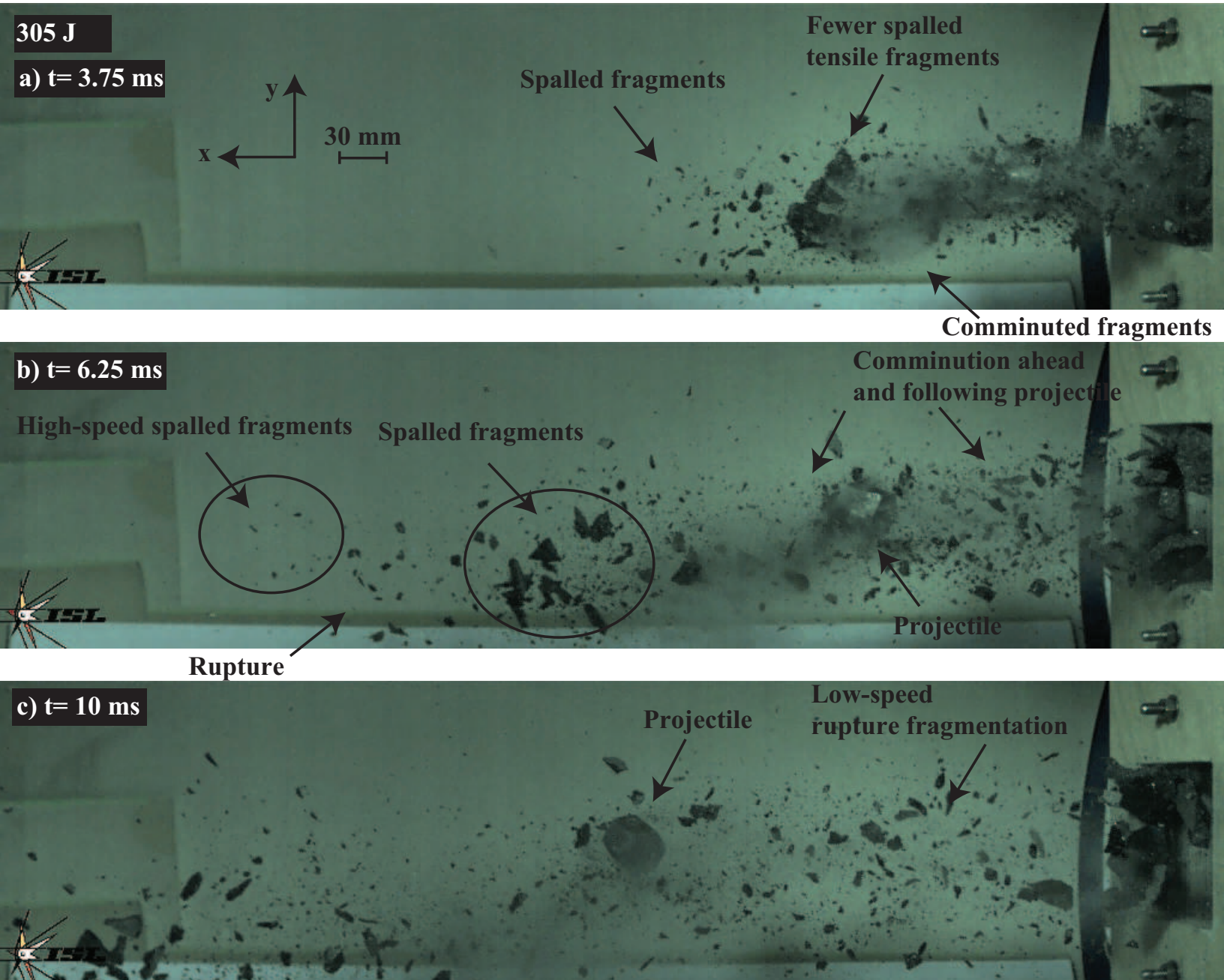

Fig4 Target images

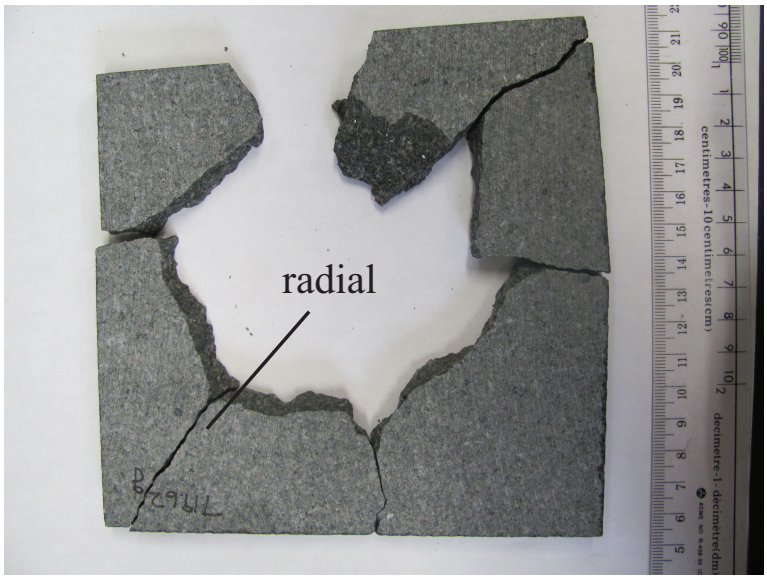

a)

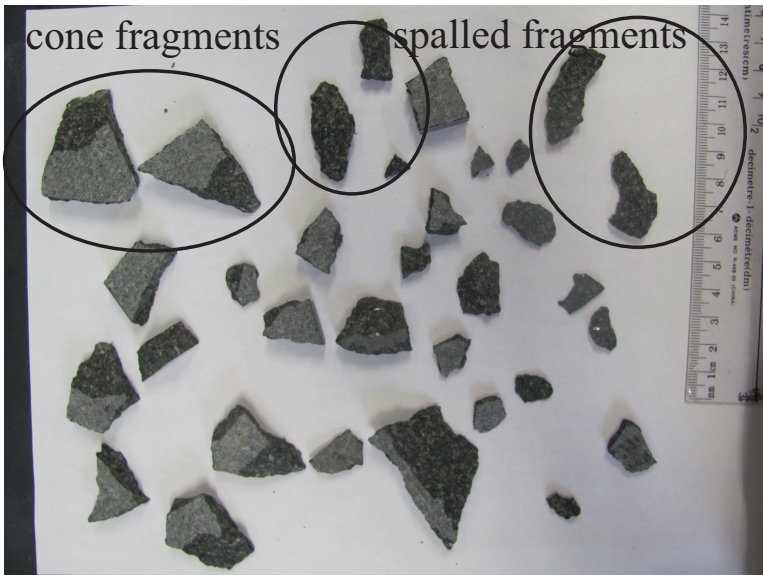

b)

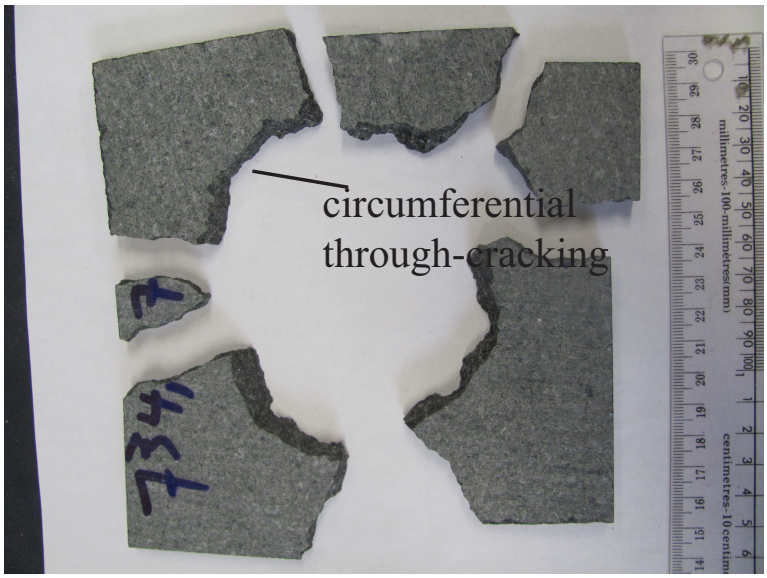

c)

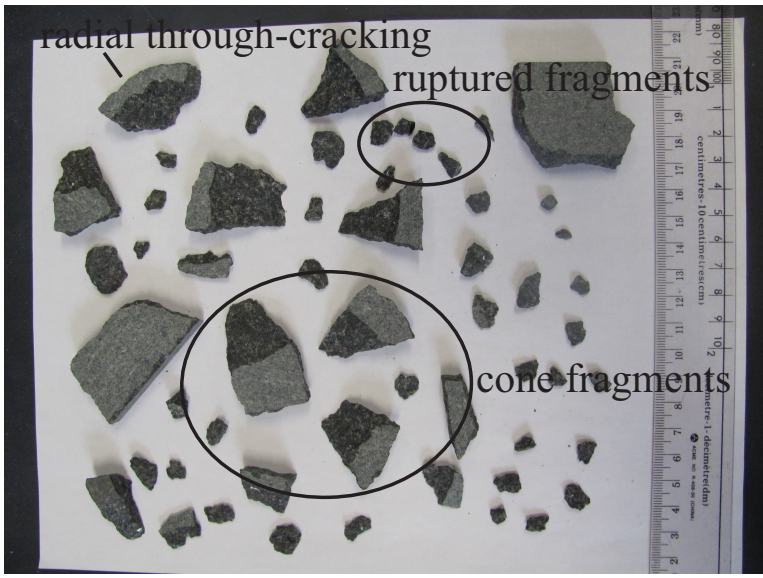

d)

Fig5 Velocity ejecta field

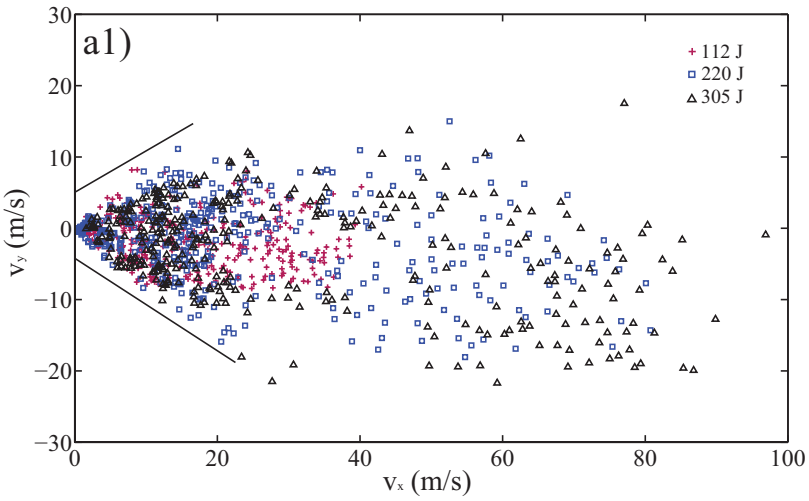

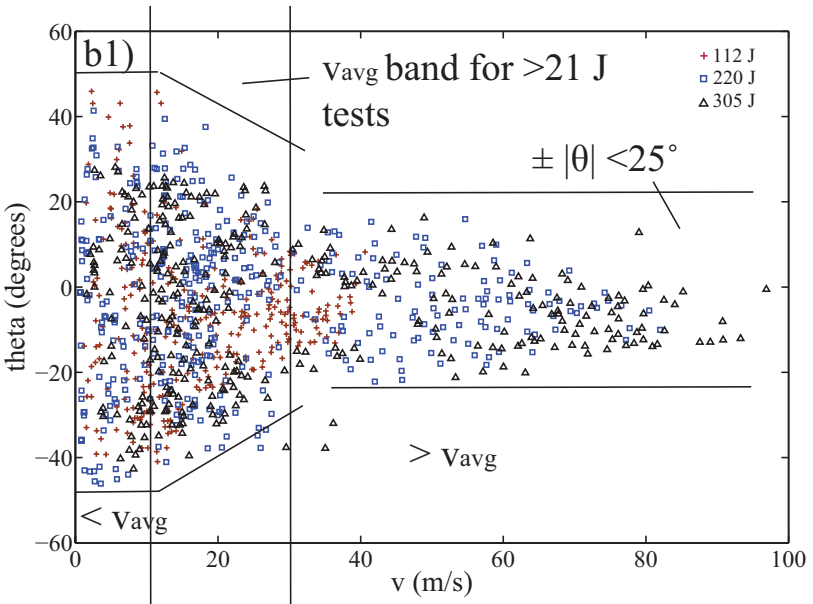

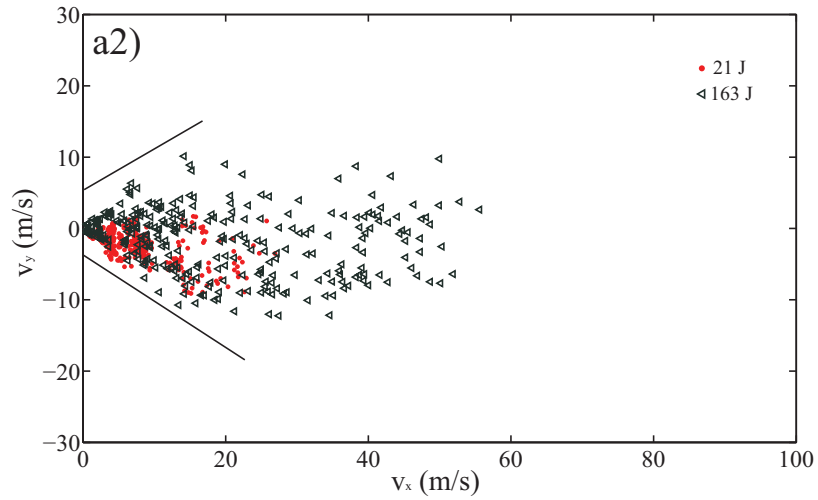

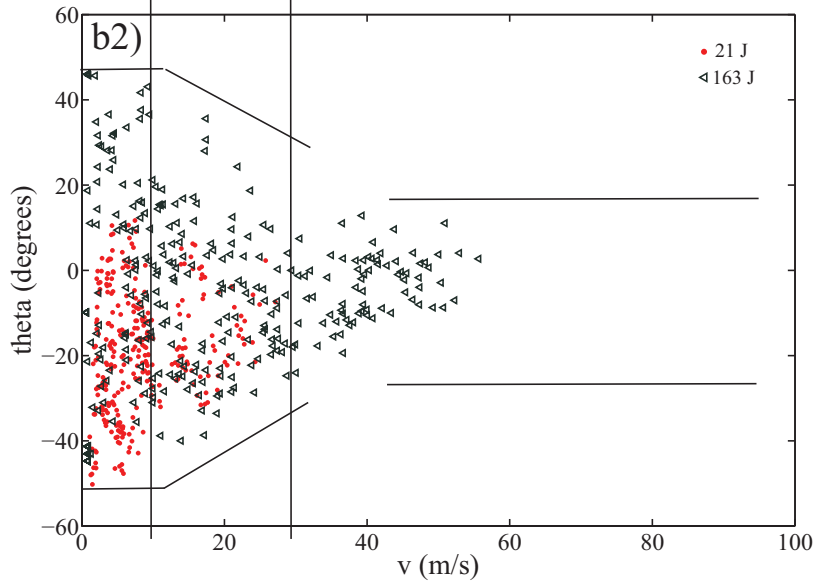

Fig6 KE of projectile post impact

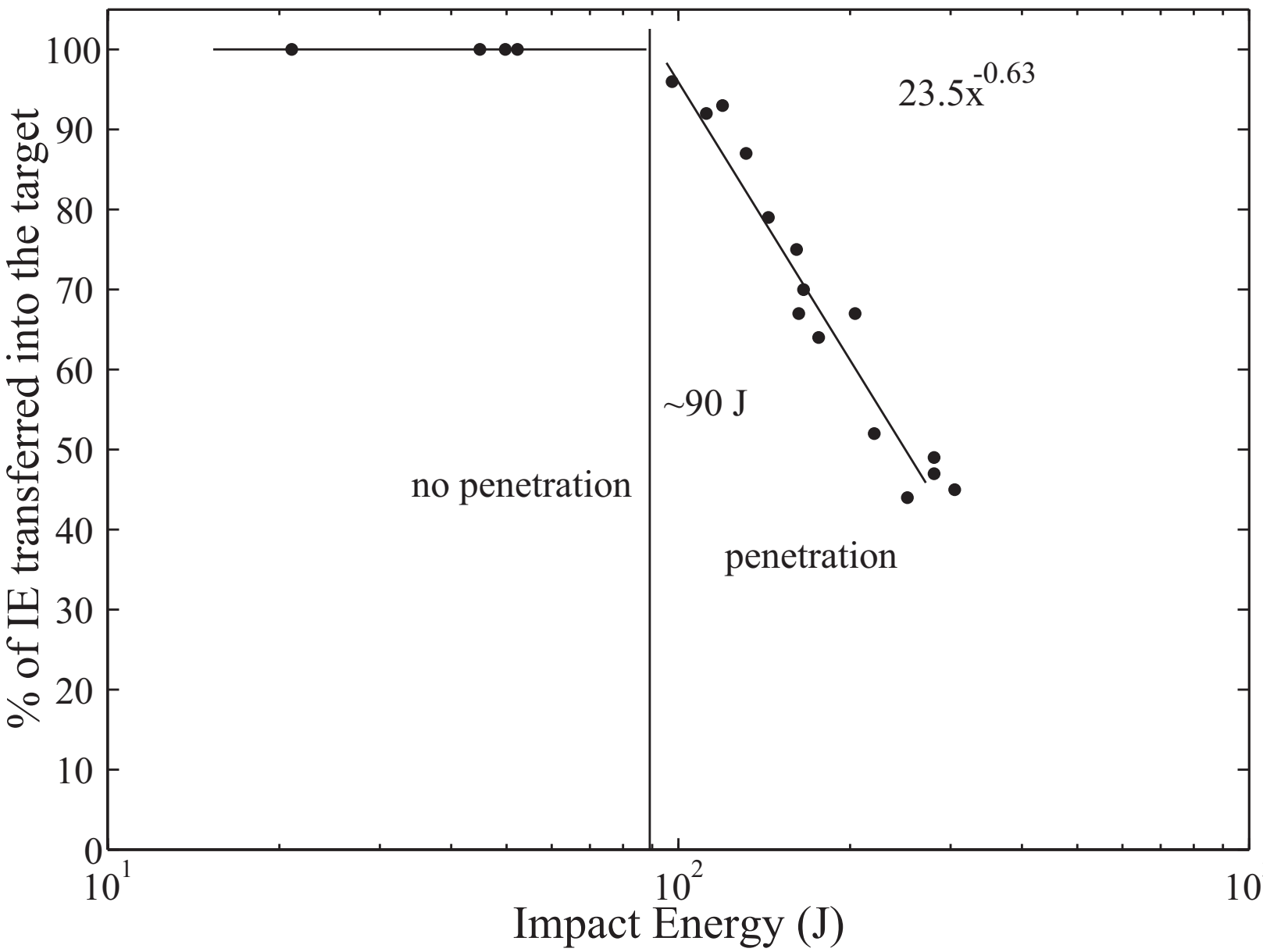

Fig7 Histogram of ejection angle

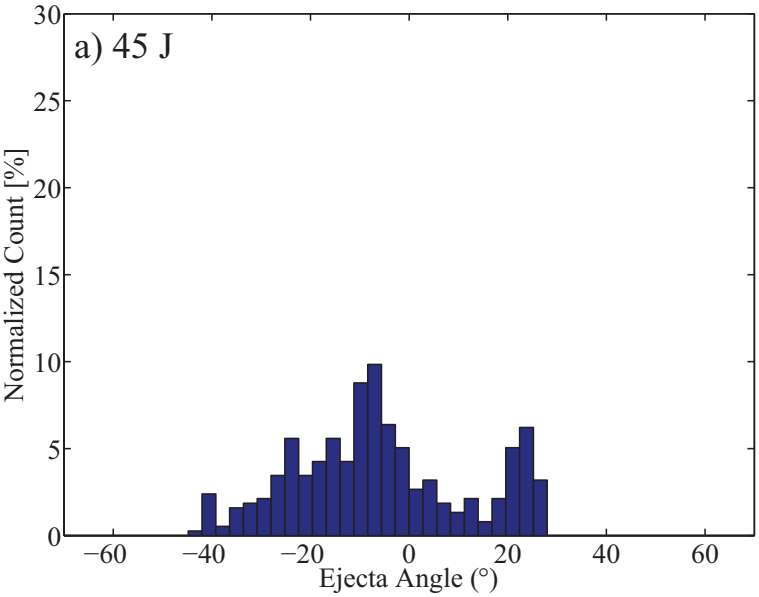

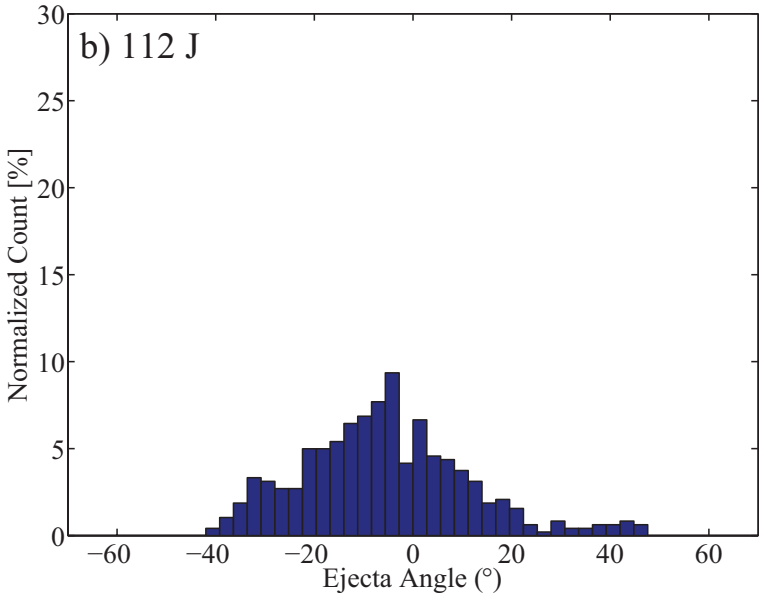

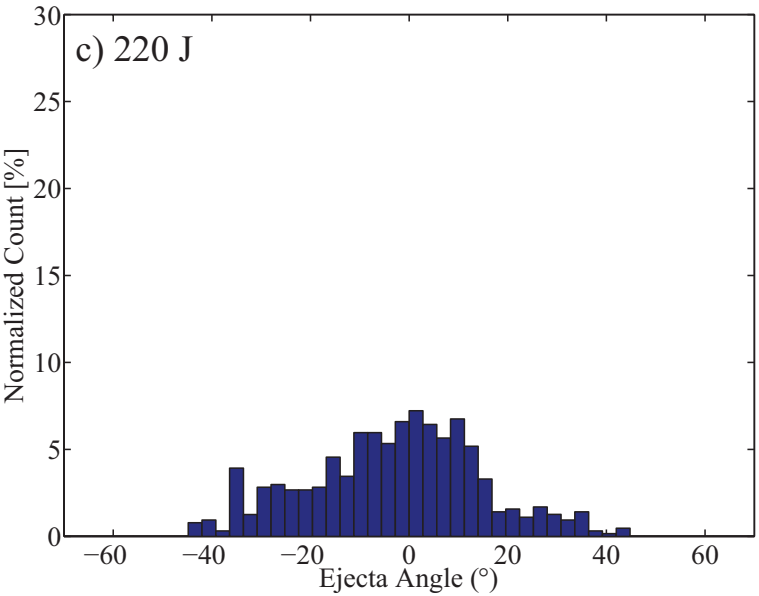

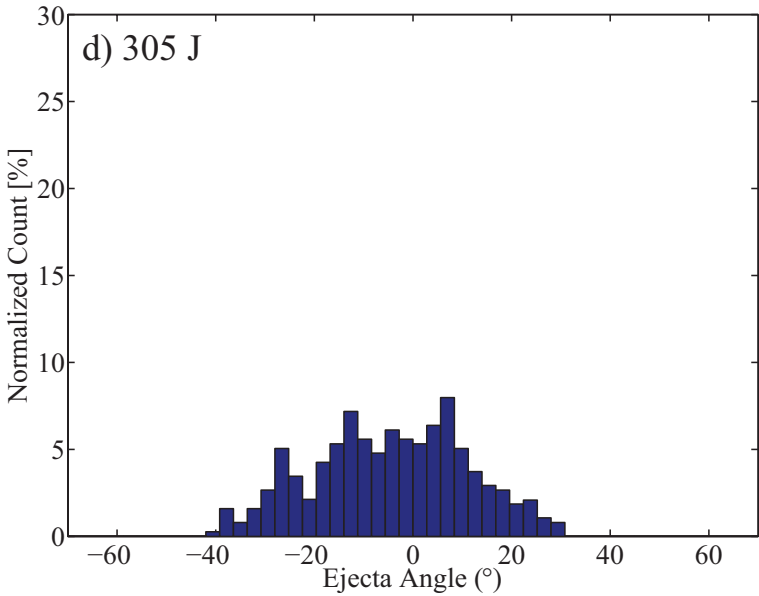

Fig8 KE distribution among ejection angles

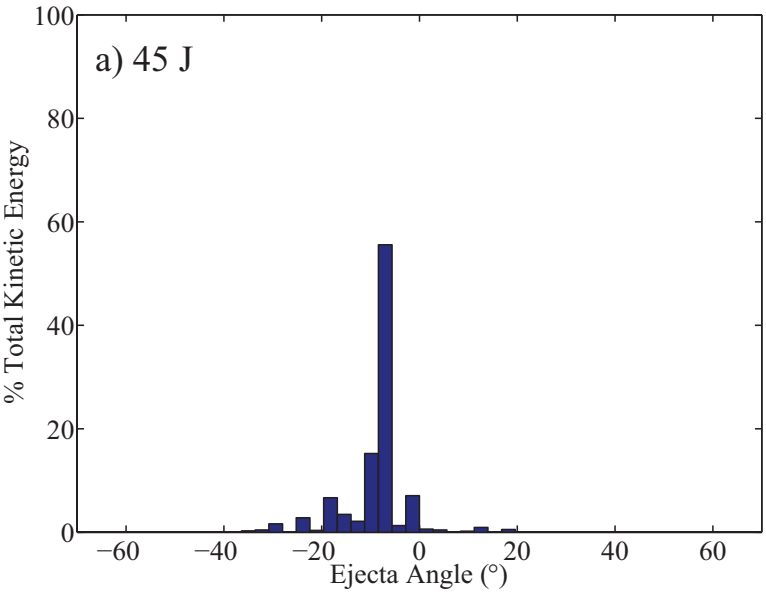

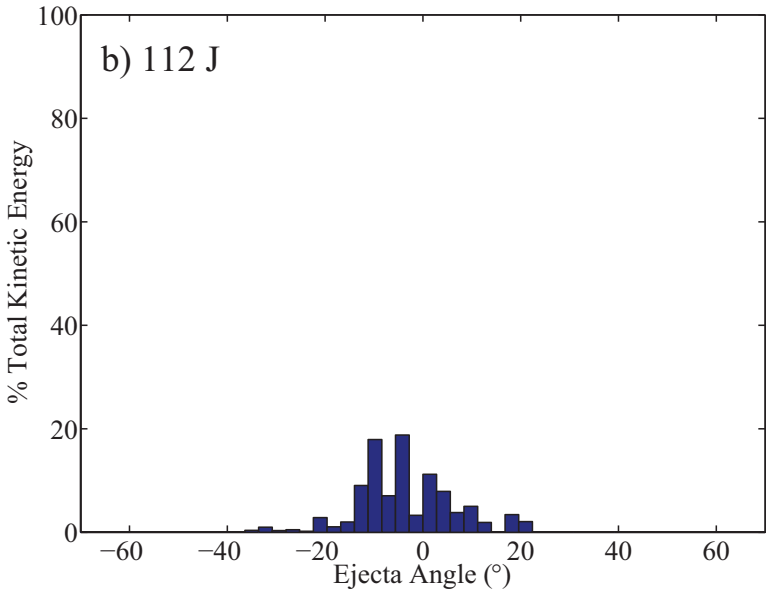

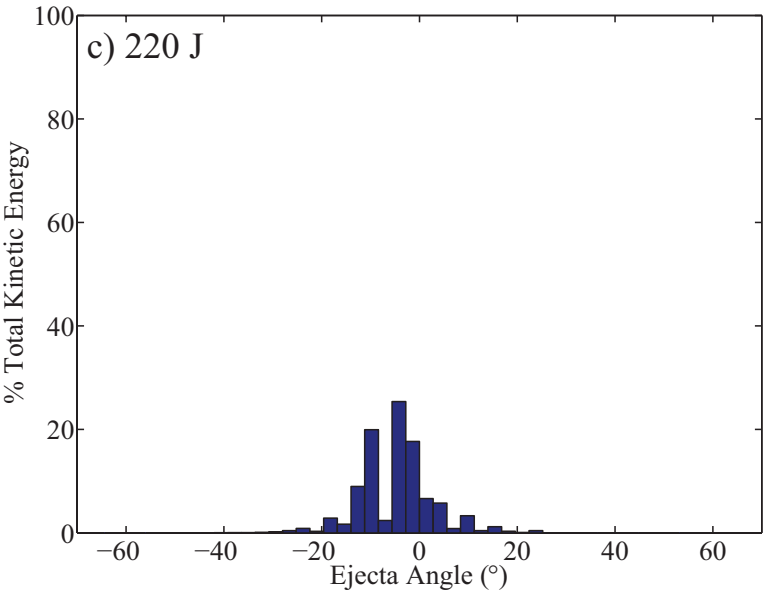

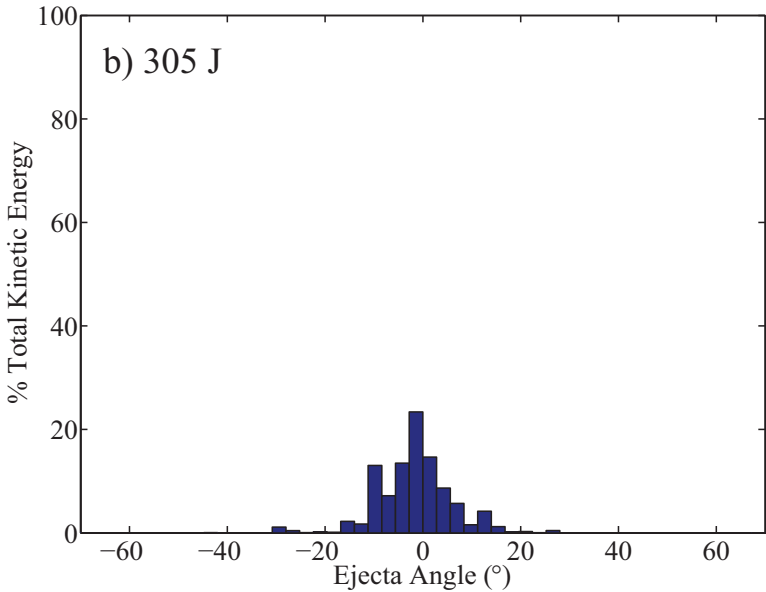

Fig9 Histogram of fragment sizes, KE to each size, and mass

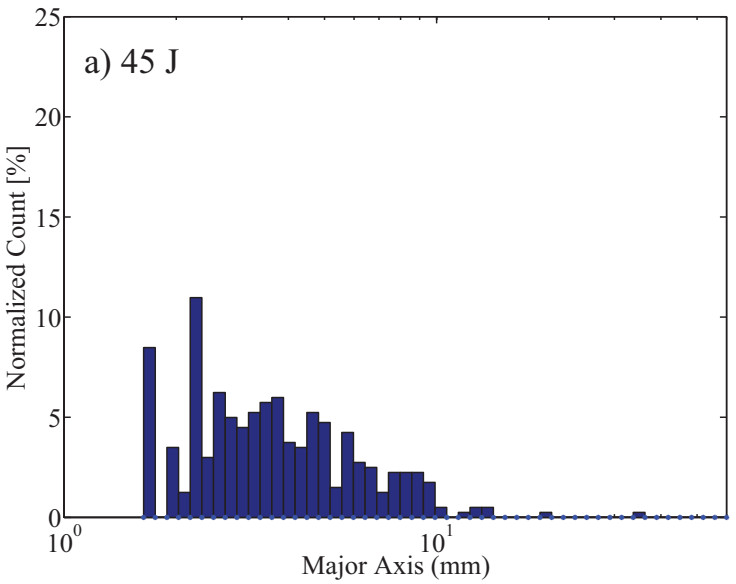

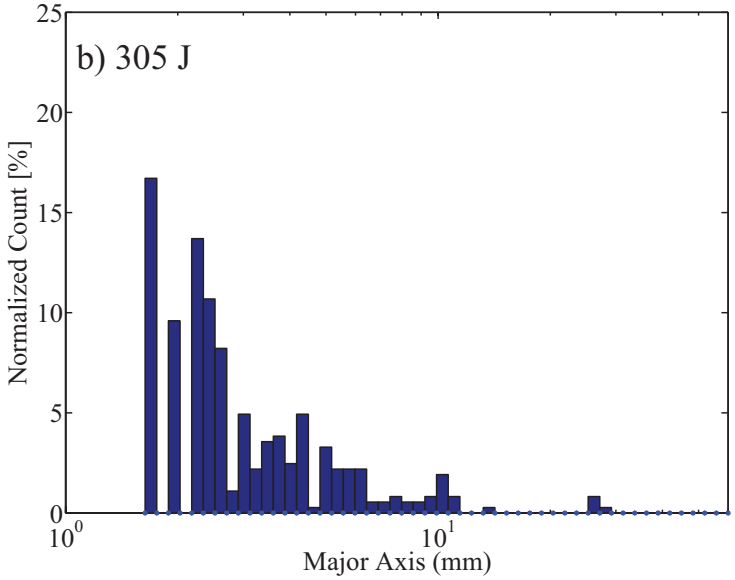

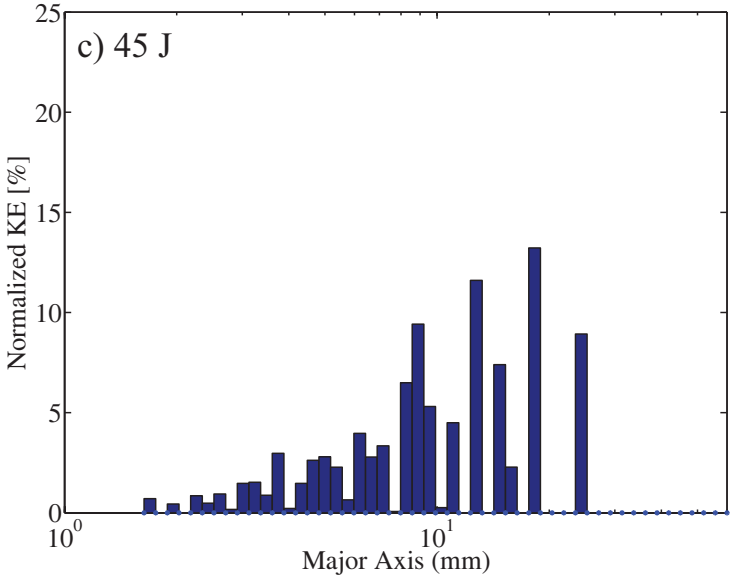

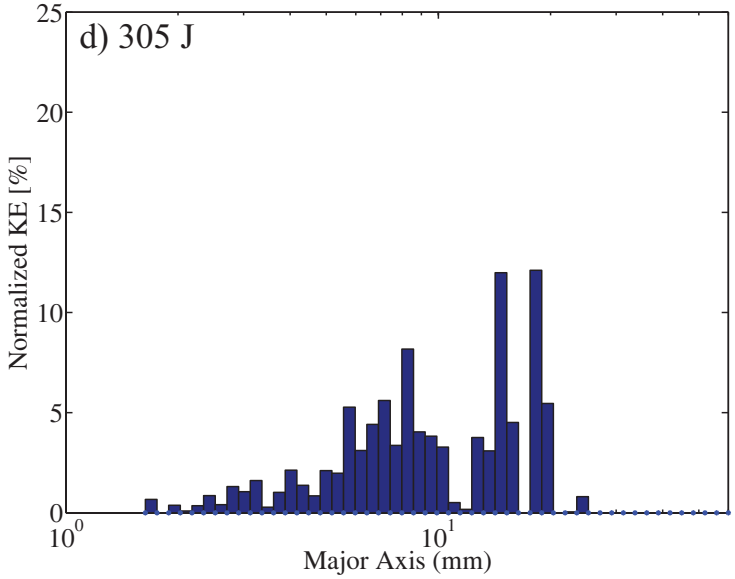

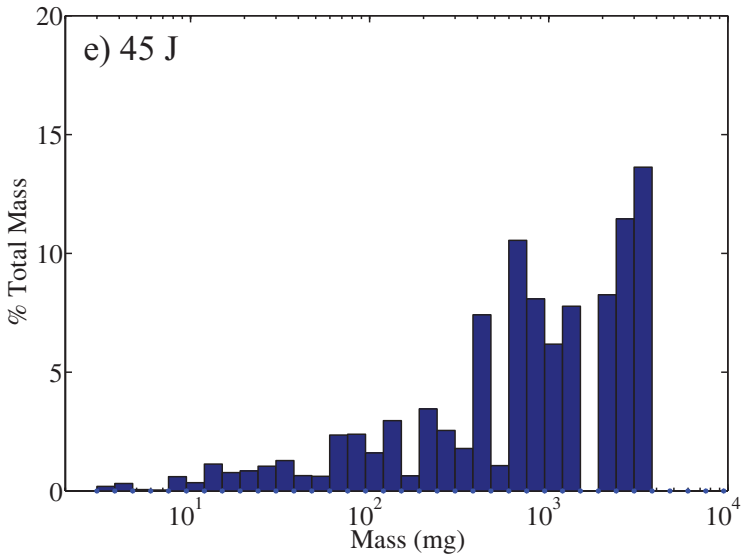

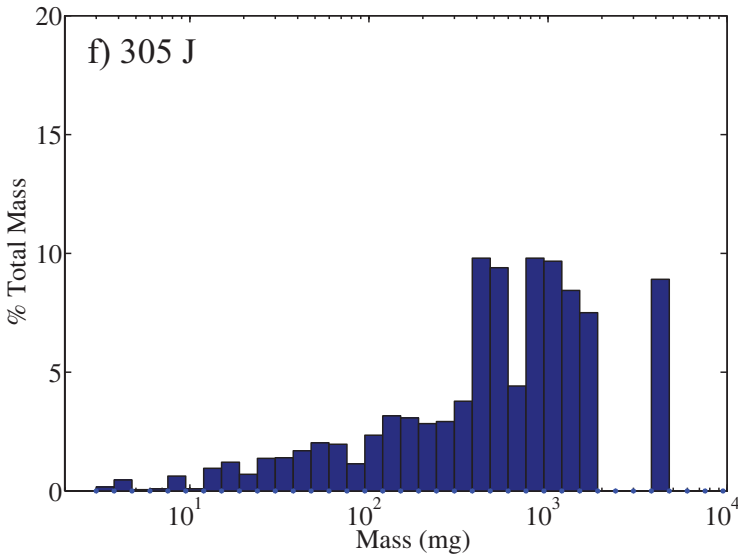

Fig10 Histogram distribution of ejecta velocity

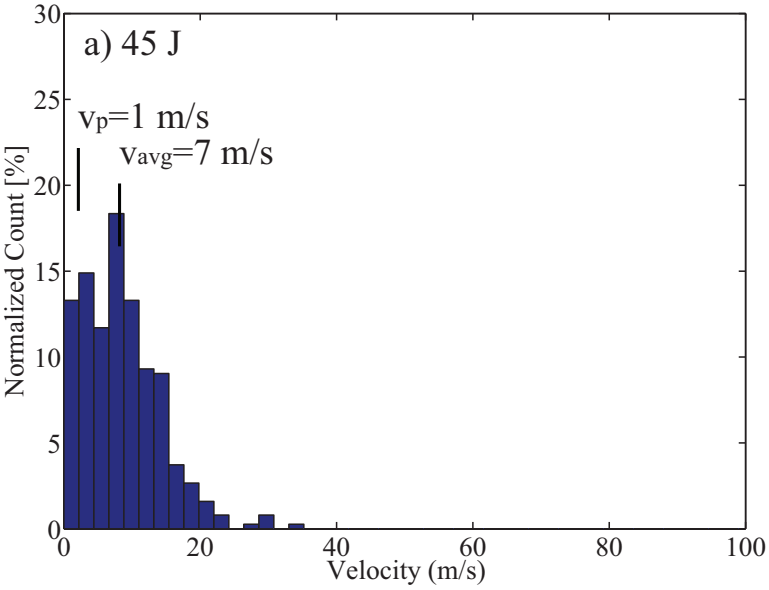

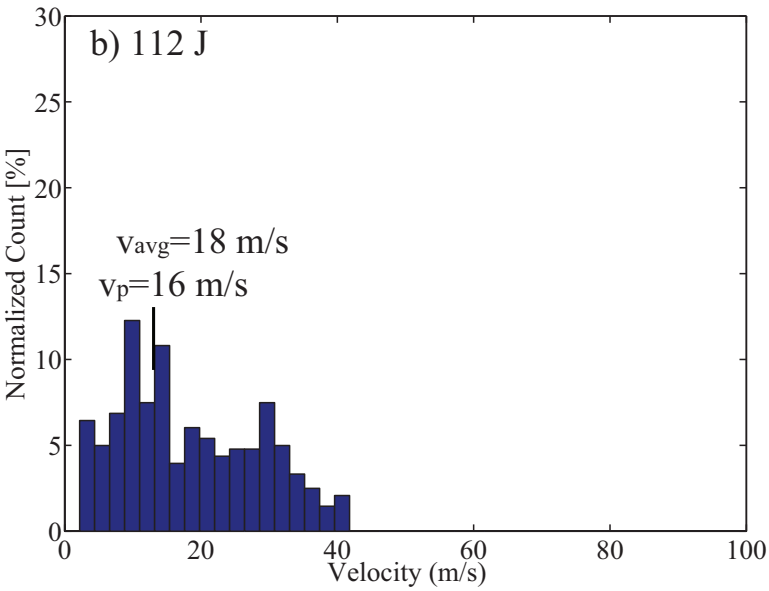

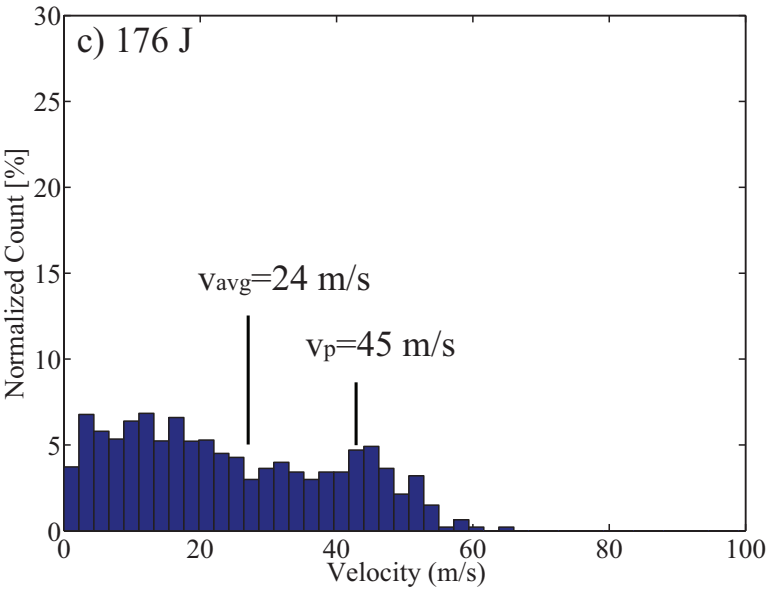

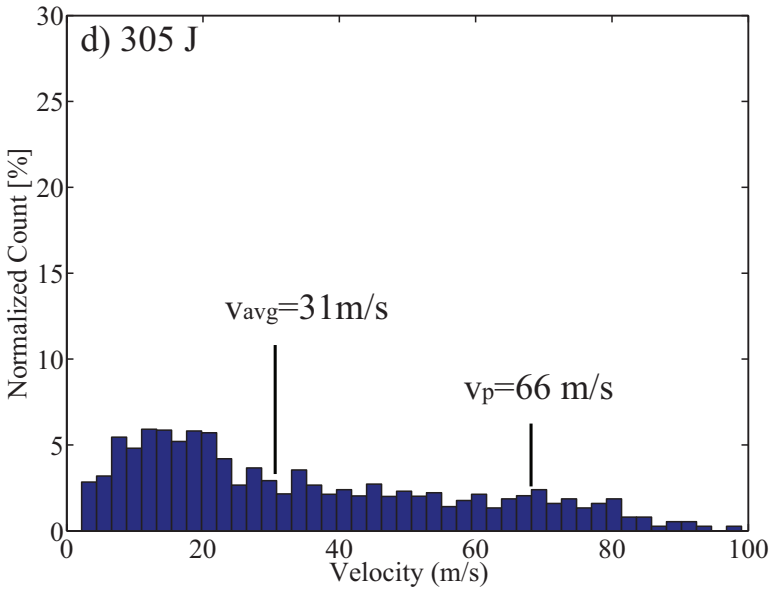

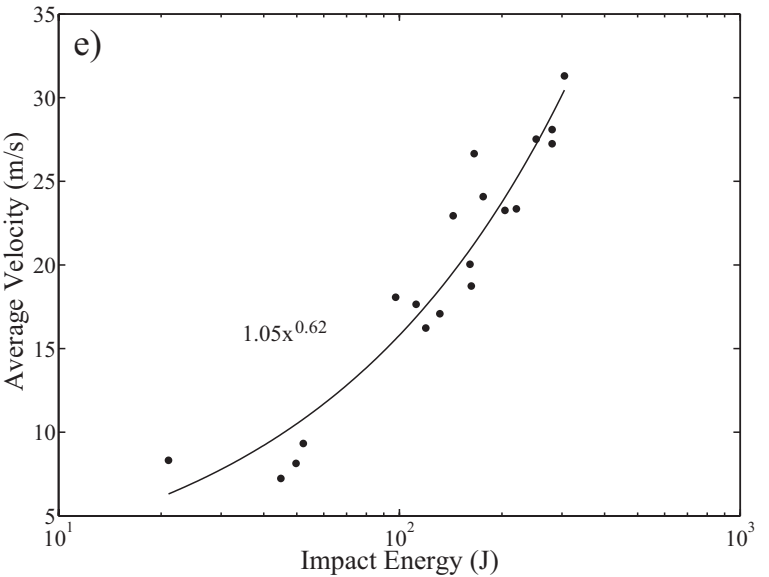

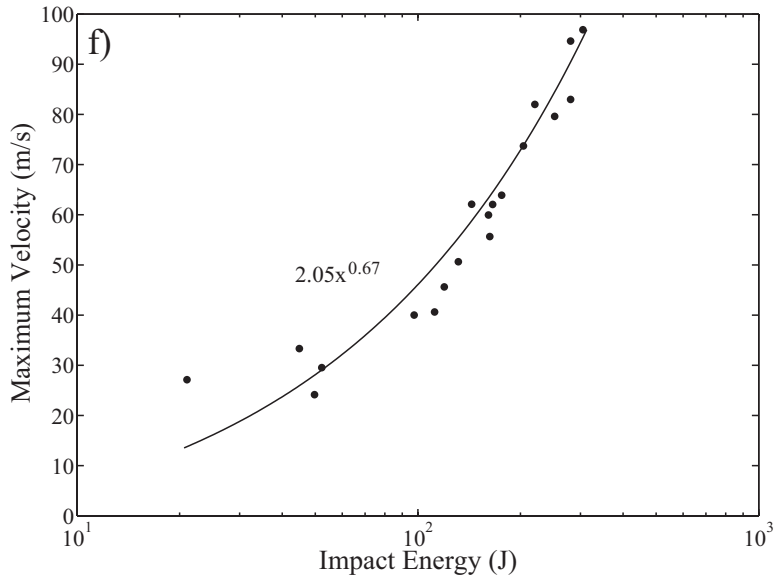

Fig11 Distribution of KE among ejecta velocity

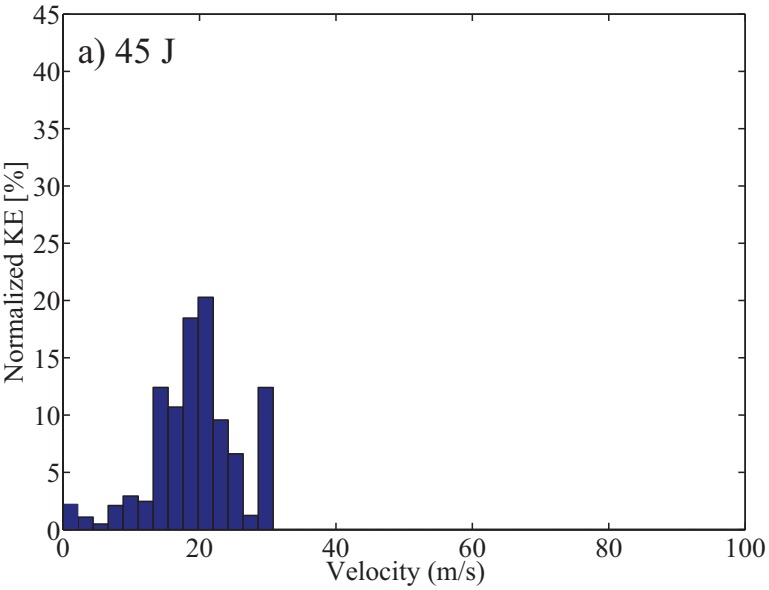

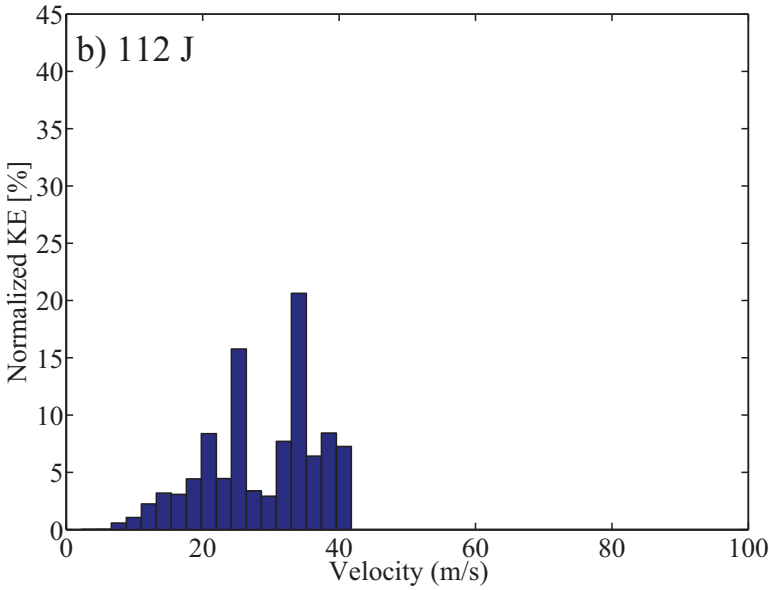

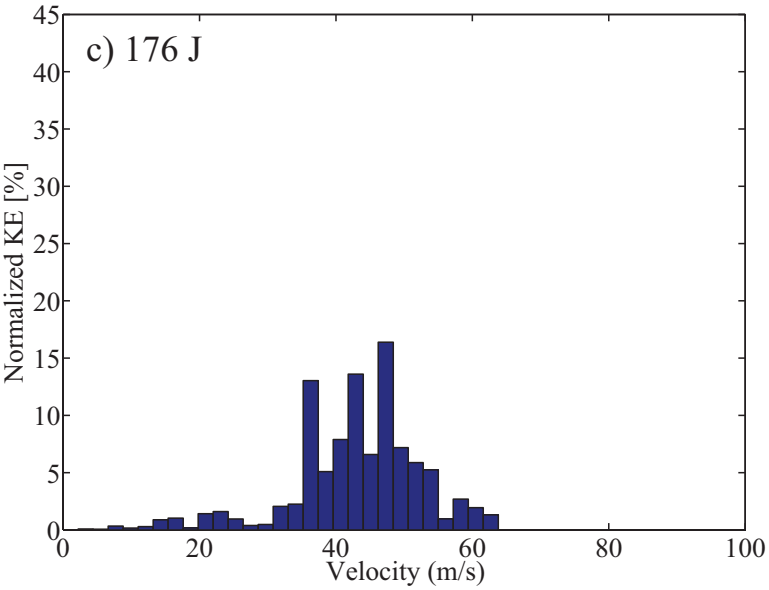

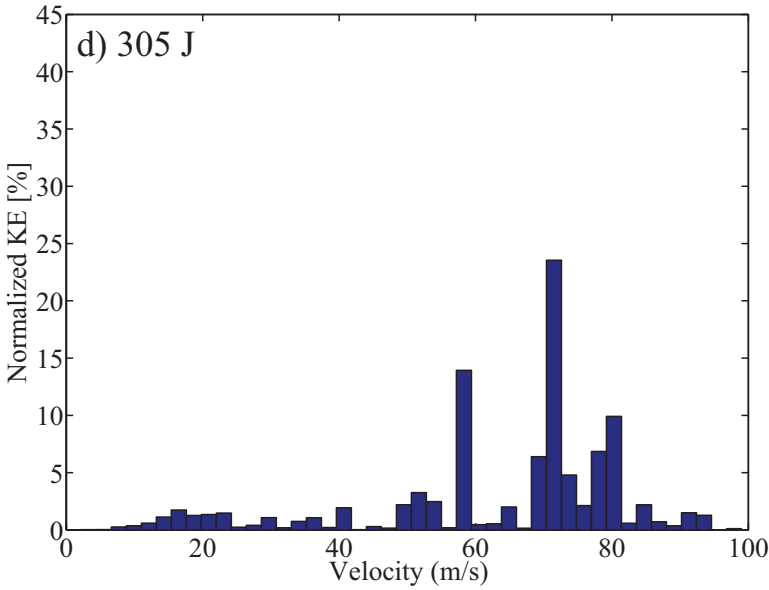

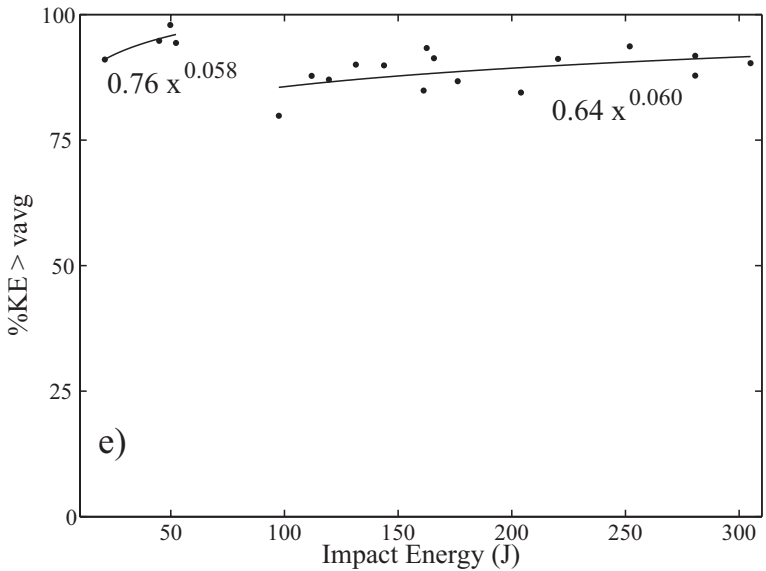

Fig12 Histogram distribution of KE

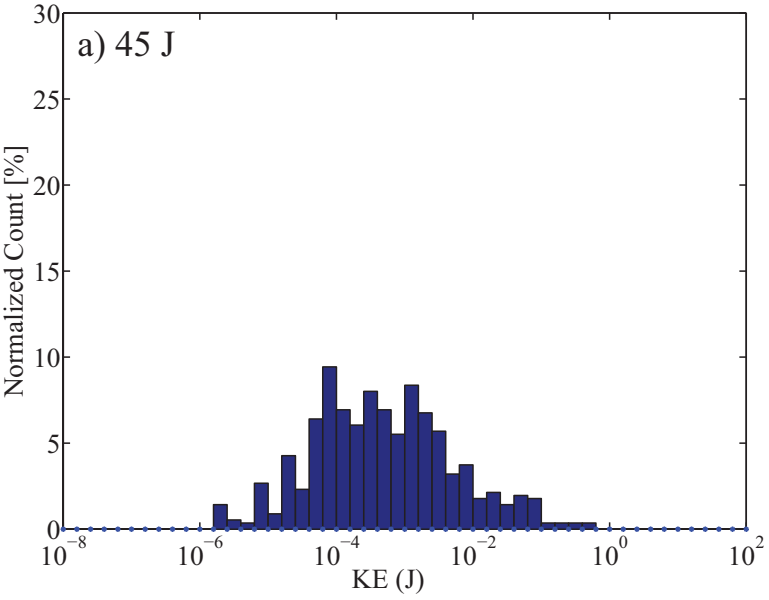

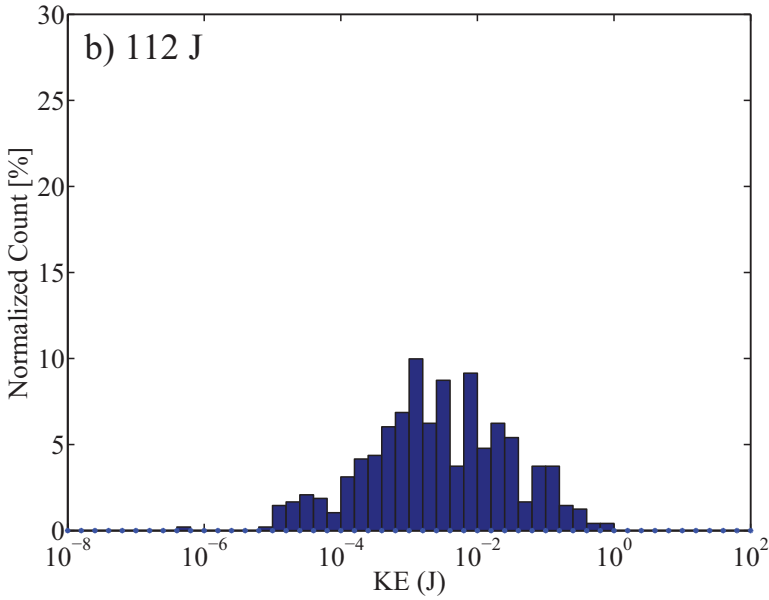

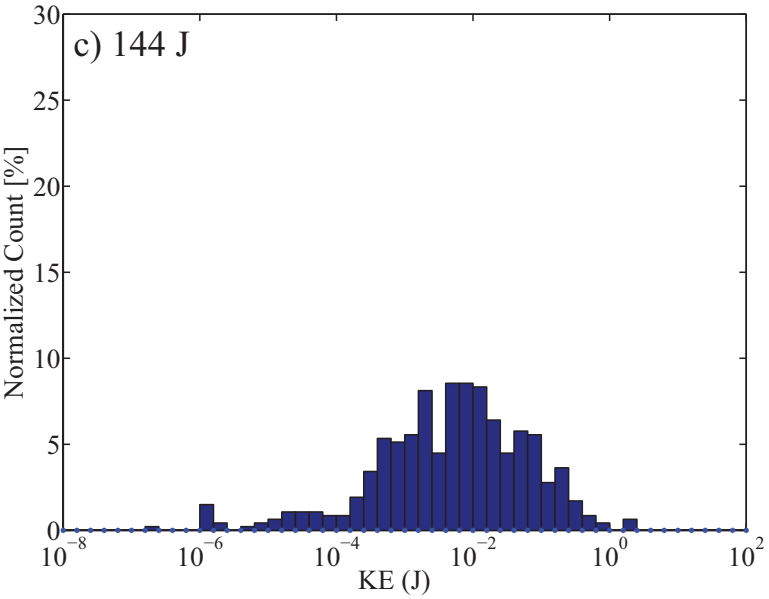

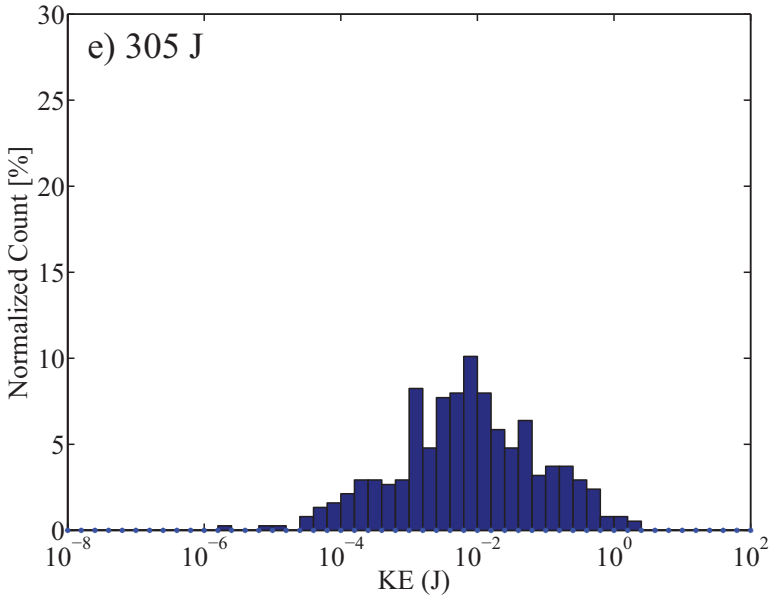

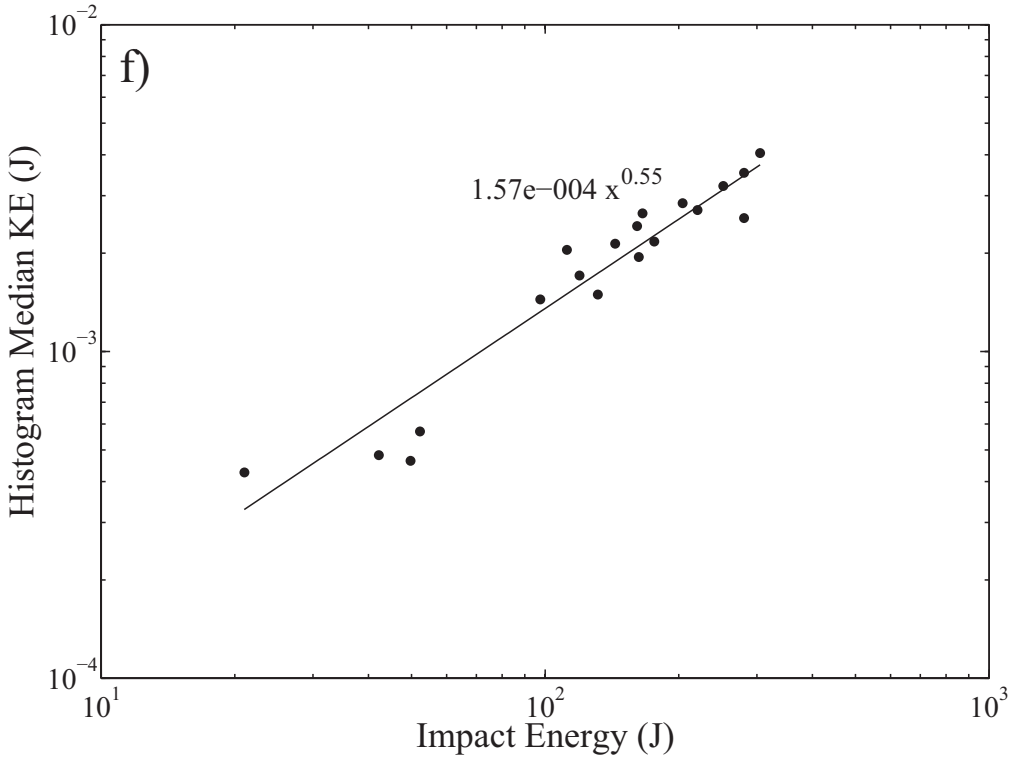

Fig13 KE distribution with KE and total % KE and % Momentum

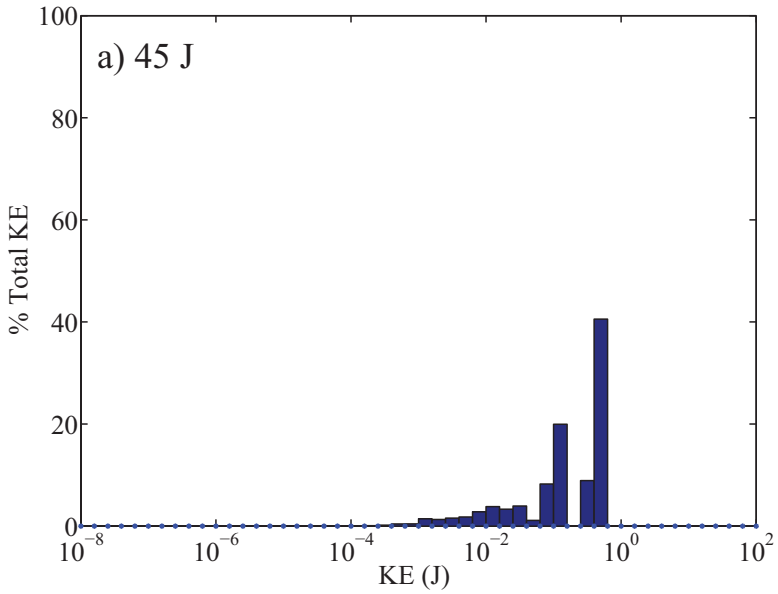

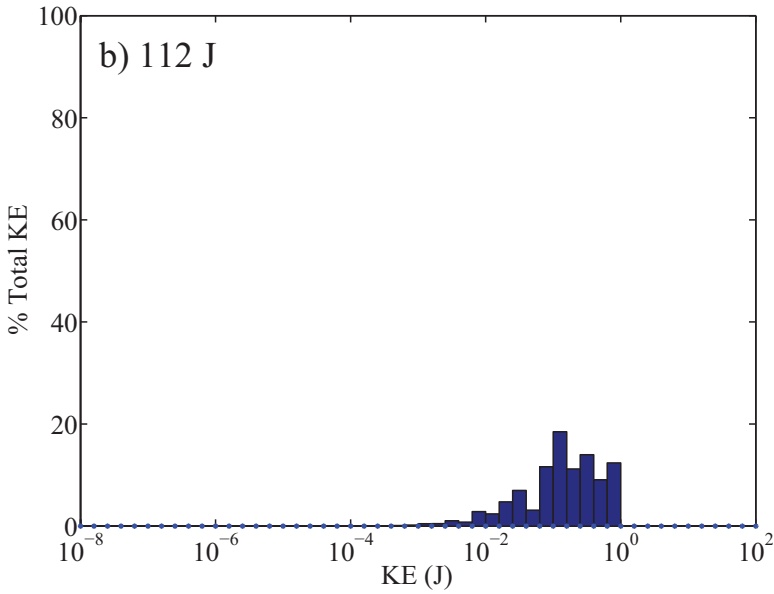

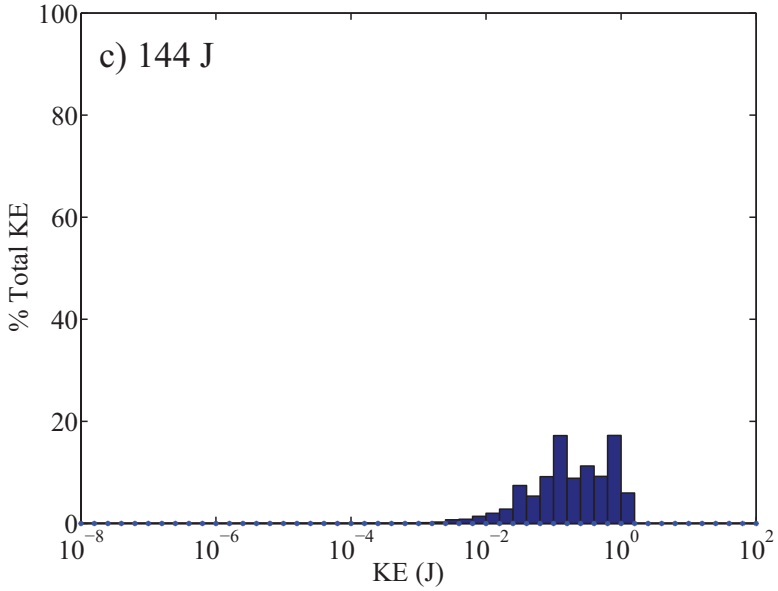

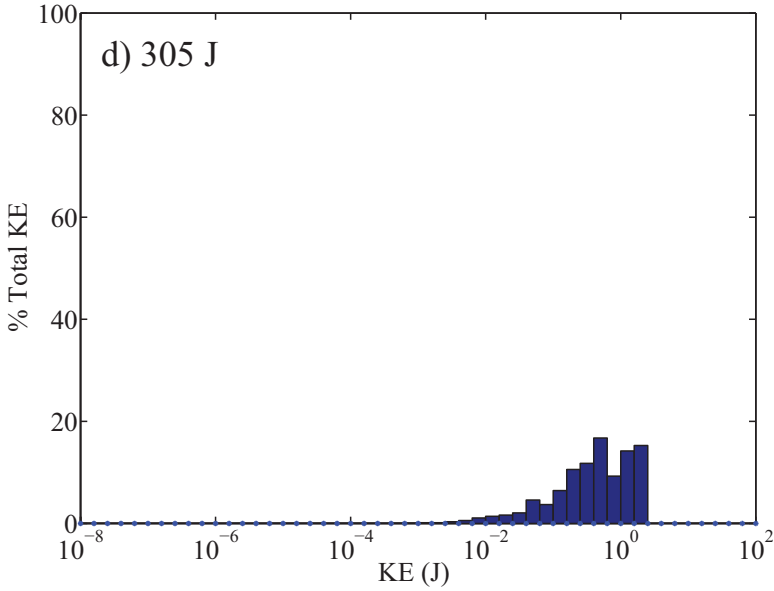

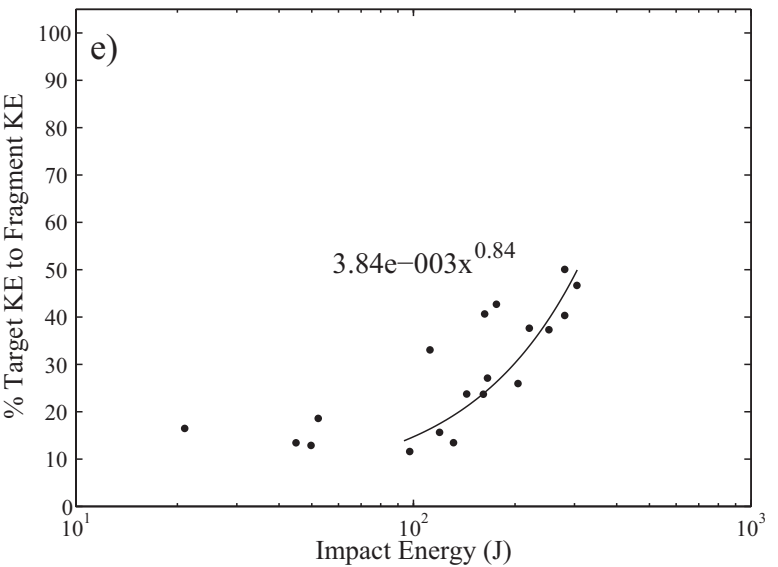

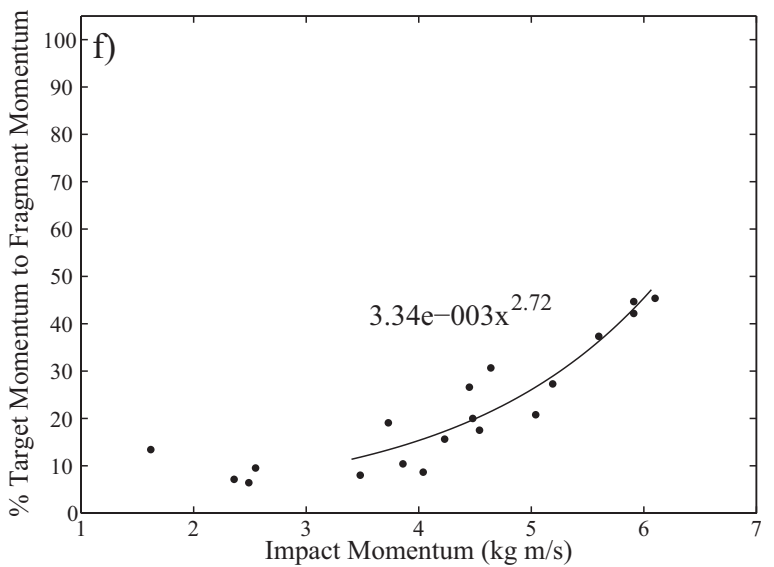

Fig14 SEM images of fracture surfaces

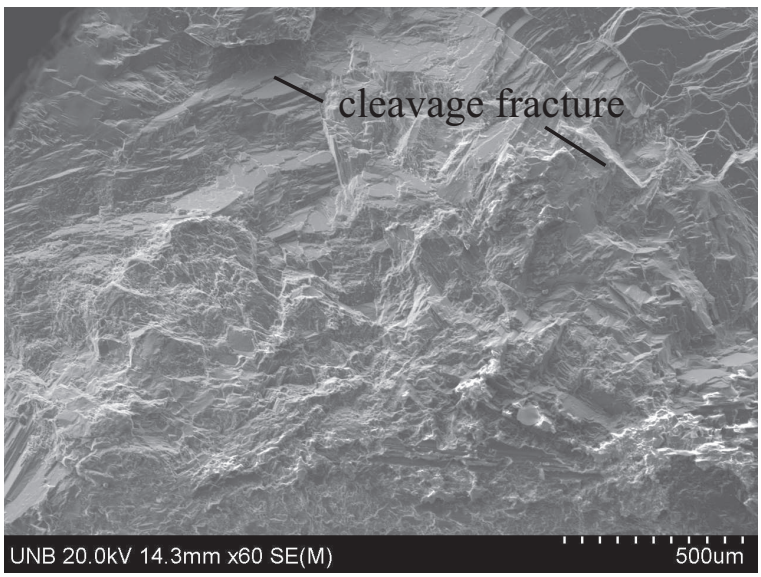

a)

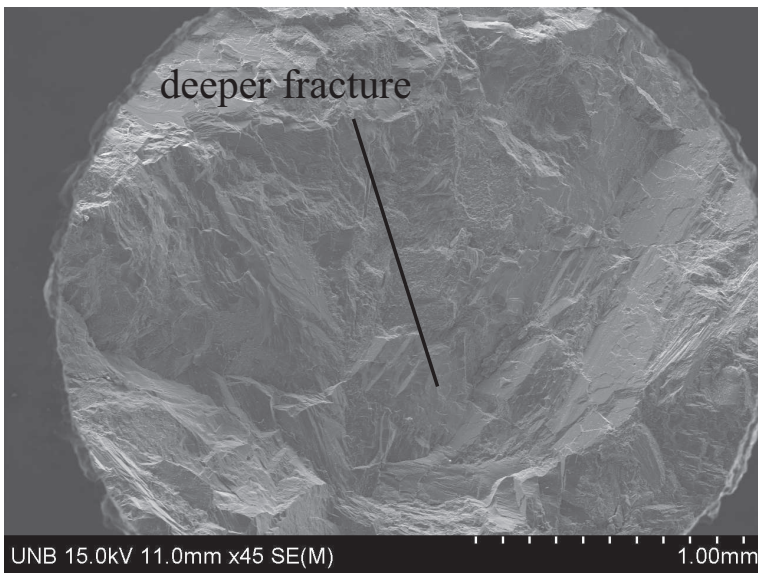

b)

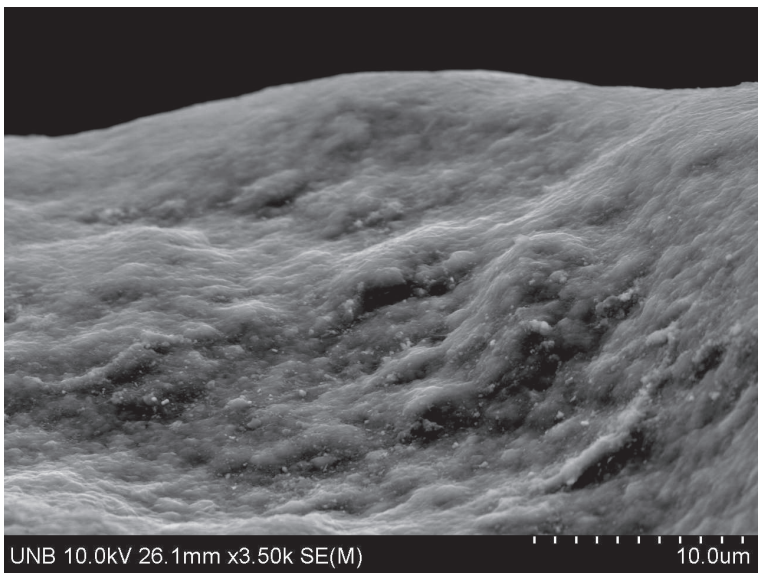

c)

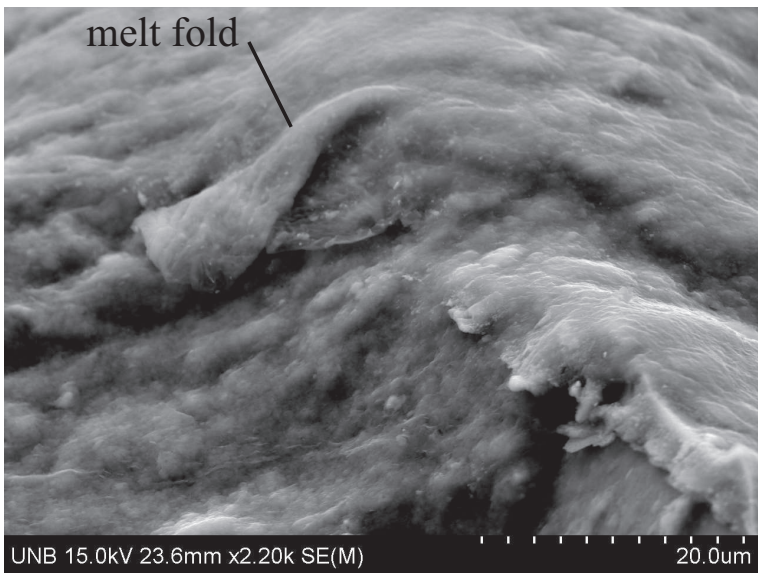

d)

Fig 15 SEM images of intra-fragment fracture features

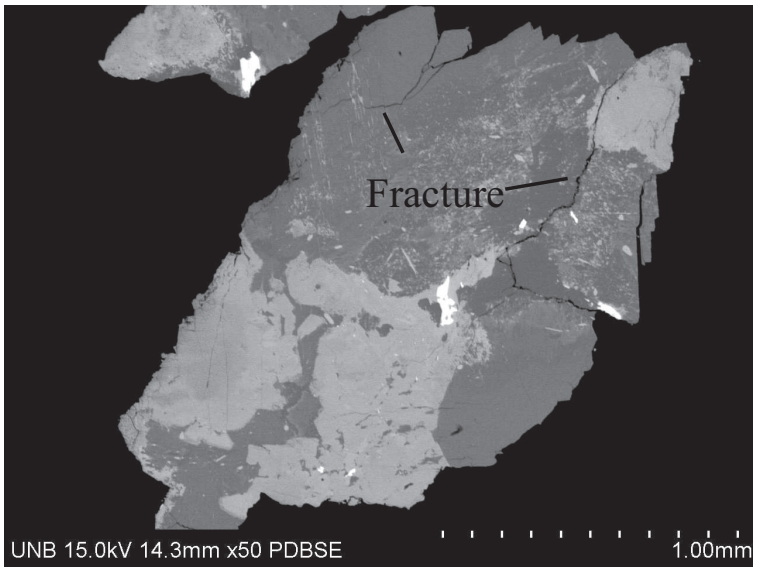

a)

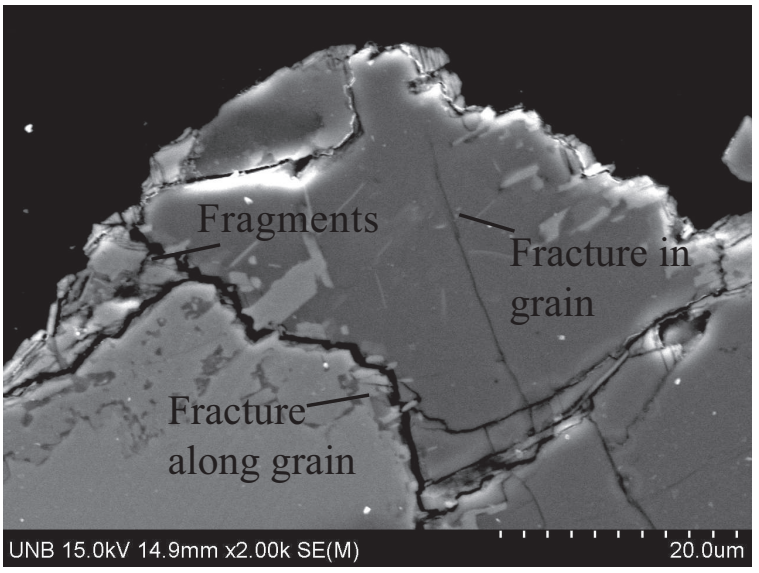

b)

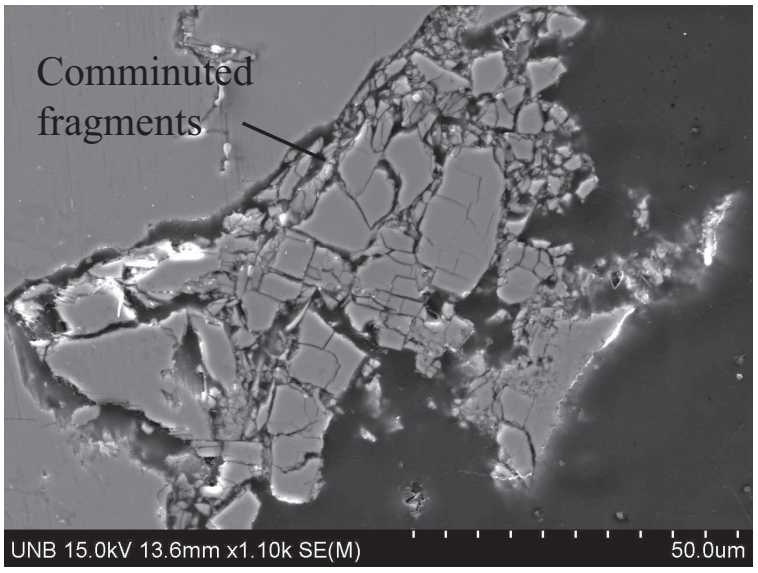

c)

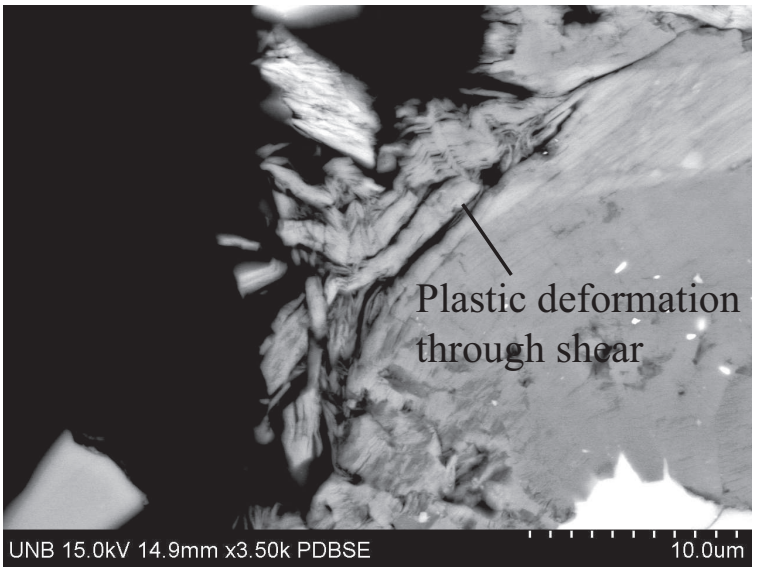

d)

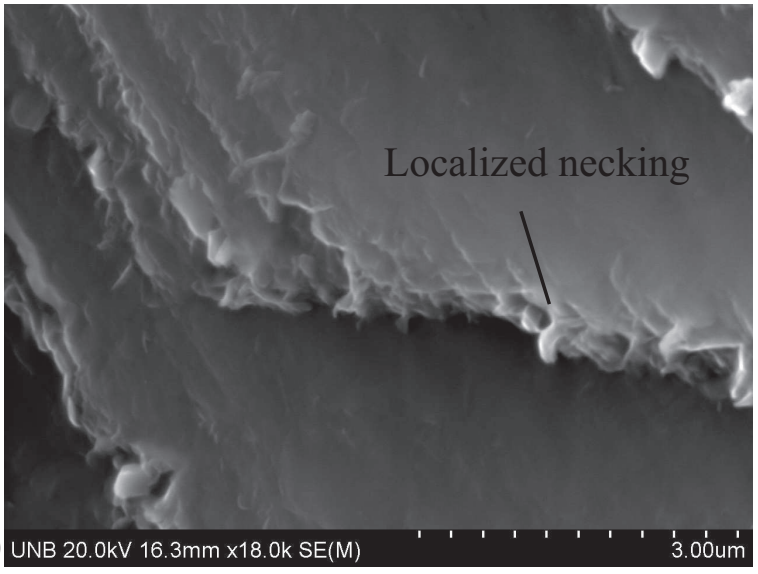

e)

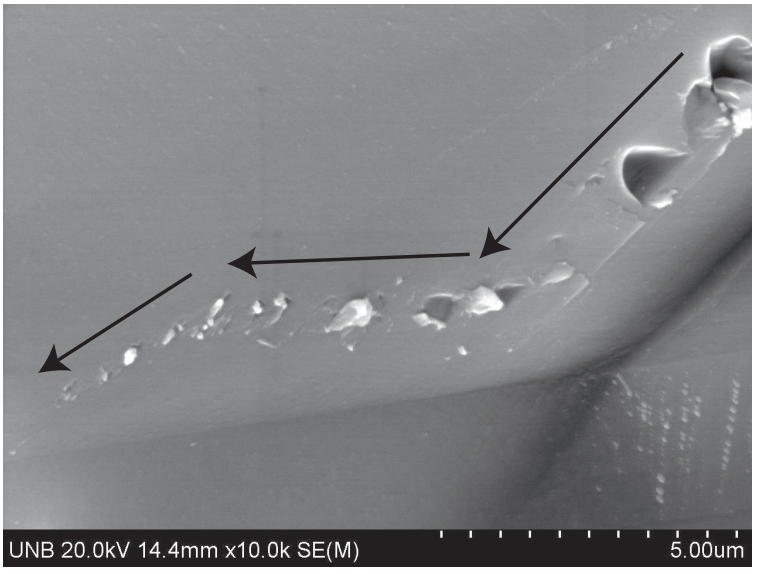

f)